OBSERVATIONS ON THE MAGNETIC IRON OXIDE CONTENT OF PARTICULATE MATTER IN THE SAHEL

by

Kimberly Belle Tidd

May 2019

THESIS

Submitted in partial fulfillment of the requirements

for the degree of Master of Science in Geology
at The University of Texas at Arlington

May, 2019

Arlington, Texas

Supervising Committee:

Dr. Andrew Hunt, Supervising Professor
Dr. Hyeong-Moo Shin
Dr. James Grover

Abstract

OBSERVATIONS ON MAGNETIC IRON OXIDE CONTENT OF PARTICULATE MATTER IN THE SAHEL

Kimberly Belle Tidd, M.S.
The University of Texas at Arlington

Supervising Professor: Dr. Andrew Hunt

Atmospheric dust influences many processes throughout the biosphere, hydrosphere, and atmosphere, most notably the climate, marine productivity, and human health. Recognizing the physicochemical characteristics of dust particulates will assist with monitoring the changes brought on by dust storms, as well as changes that may occur if dust subsides. Munsell soil color analysis was used to identify the degree of weathering at sample collection sites from the Sahel, a climate-sensitive region of North Africa. Scanning electron microscopy and energy dispersive x-ray spectroscopy were used to obtain the size, shape, and elemental makeup of individual magnetic metal particulates. Samples examined were collected along a west-east transect through Niger and Chad. No trends were found along the transect for soil color, particle physicochemistry, degree of weathering, or amount of precipitation of new minerals. Among the particles were iron oxides, iron-titanium oxides, and titanium oxides that exhibited weathering and precipitation features expected of the sample area. Several grains showed both dissolution and precipitation at the same time, indicating a variable and sensitive environment. Several contaminants were found, implicating anthropogenic sources such as mining and road dust.

Table of Contents

List of Figures

List of Tables

Introduction

Atmospheric dust influences local and regional environmental conditions and contributes to climate change (Ginoux et al., 2012; IPCC, 2014). Biogeochemical processes affect environmental health including marine productivity, soil nutrition, and the climate (Goudie, 2014; Chien et al., 2016; Gross et al., 2016; Middleton, 2017). Dust negatively impacts human health and the economy (Ginoux et al., 2012; IPCC, 2014; Gherboudj et al., 2017; Middleton, 2017). Understanding the generation, transportation, and deposition of aerosol particles is necessary to evaluate the effects of dust emissions (Grousset and Biscaye, 2005; Gross et al., 2016). Recognizing the geochemical properties of dust and source region lithology can assist models to assess future environmental impacts (Grousset and Biscaye, 2005; Shao et al., 2011; Gross et al., 2016).

Dust contributes to marine health by providing phytoplankton with necessary nutrients phosphorus and iron (Okin et al., 2011; Chien et al., 2016). Too much dust input has been attributed to the development of bacterial blooms (Pulido-Villena et al., 2008; Westrich et al., 2016), algal blooms (Goudie, 2014; Al Shehhi et al., 2014), and red tides (Walsh et al., 2006; Lenes et al., 2008; Goudie, 2014). Crustal elements and spores in atmospheric dust have been shown to contribute to coral reef decline (Shinn et al., 2000). Dust brings nutrients to agricultural soils and deposits on canopies and topsoils of natural forests (Rizzo et al., 2013; Rizzolo et al., 2017). Dust storms can lead to sandblasting of crops and soil degradation (Scheuvens et al., 2013; Middleton, 2017).

Dust emissions can help or harm the local, regional, and global climate by affecting Earth's energy budget (Winckler and Mahowald, 2014; Kok et al., 2017). Atmospheric particles keep the Earth cool by scattering incoming radiation (Guiraud et al., 2005; Scheuvens et al., 2013; Winckler and

Mahowald, 2014; Bretl et al., 2015; Alamirew et al., 2018; Pan et al., 2018; Strong et al., 2018) and provides cloud condensation nuclei (CCN) and ice nuclei (IN) (Levin et al., 1985; Bretl et al., 2015; Boose et al., 2016; Amiri-Farahani et al., 2017). A reduction of dust emissions creates warmer atmosphere, thus warming the oceans (Ridley et al., 2014; Schewe and Levermann, 2017), as well as leading to drought and desertification (Zhao et al., 2011; Ridley et al., 2014; Thomas and Nigam, 2018). Numerous studies have asserted that extreme dust events can inhibit tropical cyclone formation (Dunion and Velden, 2004; Wu, 2007; Strong et al., 2018). However, more studies are needed to confirm the role dust plays in hurricane formation due to the large role it plays in various climatic functions (Bretl et al., 2015; Pan et al., 2018). Feedback loops created by dust emissions amplify effects (Maher et al., 2010; Mahowald, 2011; Zhao et al., 2011; Ridley et al., 2014; Williams et al., 2016; Schewe and Levermann, 2017; Alamirew et al., 2018).

Atmospheric dust reduces air quality, causing widespread damage to human health (Ozer et al., 2007; Prospero et al., 2008; De Longueville et al., 2010; Goudie, 2014; Prospero et al., 2014b; Middleton, 2017). Allergens, pathogens, bacteria, viruses, pollen, and fungi in dust storms can be carried over long distances and have far-reaching health effects (Kellogg and Griffin, 2006; Griffin, 2007; Coz et al., 2011; Smith et al., 2012). Particulate matter (PM) of all sizes affects human health in different ways (Goudie, 2014). Coarse PM can increase asthma issues and increase the number of respiratory and cardiovascular admissions to hospitals (Brunekreef and Forsberg, 2005; Akpinar-Elci et al., 2015). Particulate matter with an aerodynamic diameter in the range 2.5-10 μm (PM10) can increase asthma issues and cause mortality (Díaz et al., 2012; Lee and Lee, 2013; Ortiz-Martínez et al., 2015). Particulate matter with an aerodynamic diameter $\leq$2.5 μm (PM2.5) can cause lung inflammation, as well as cardiovascular morbidity and mortality (Brunekreef and Forsberg, 2005; Giannadaki et al., 2014; Rodríguez-Cotto et al., 2015).

Additionally, physicochemical changes during transport can cause additional complications. Dust particles may become condensation nuclei for natural and anthropogenic pollutants (Coz et al., 2011; Rizzo et al., 2013).

Economic issues can arise from dust storm activity (Middleton, 2017). Dust storms damage machinery and solar panels, and reduce visibility (Scheuvens et al., 2013; Gherboudj et al., 2017). Wind erosion can be increased because of poor farming practices, thus degrading soil quality, stripping crops, and leading to desertification and drought (Middleton, 2017). Additionally, dust storms cause transport accidents and flight disruptions (Goudie, 2014; Middleton, 2017).

Mineral dust interacts in multiple ways with the atmosphere, biosphere, and hydrosphere (Chou et al., 2008; Formenti et al., 2011; Formenti et al., 2014b; Rocha-Lima et al., 2018). Differences in mineral physicochemical properties have implications for numerous biogeochemical systems (Waeles et al., 2007; Winckler and Mahowald, 2014; Jickells et al., 2016). Weather, climate, and circulation models use these characteristics to identify the source of atmospheric dust emissions and the processes that effect their initial properties (Kinne et al., 2010; Scheuvens et al., 2013). However, as mineral dust is generated it may experience a variety of geochemical changes that will mask or eliminate its source identity (Ridley et al., 2014). Once a rock or paleosol is exhumed, mechanical and chemical weathering may alter the original mineral constituents, thus complicating the parameters of prediction models (Lyons et al., 2012; Beauvais and Chardon, 2013; Gross et al., 2016; Hunt et al., 2017). Additionally, entrained particles undergo additional physical and chemical changes during transport within the atmosphere (Desboeufs et al., 1999; Journet et al., 2008; Scheuvens et al., 2013; Friese et al., 2017). Establishing physicochemical properties of atmospheric dust samples may assist with the identification of their source (Shao et al., 2011; Aarons et al., 2013; Kumar et al., 2018). Understanding the processes that affect particle

morphology from source to sink will be essential for many prediction models (Shao et al., 2011; Evan et al., 2015).

Physicochemical properties of mineral dust include size, composition, and shape that are characteristic of their source and transport methods. The size of a particle is a function of the topography (Washington et al., 2006b; Crouvi et al., 2012), surface wind speeds (Miller et al., 2006; Washington et al., 2006b; Washington et al., 2009; Schepanski et al., 2014), and soil roughness (Cowie et al., 2013; Gherboudj et al., 2017) of its source area. Mechanical weathering will break up larger particles (Bullard et al., 2004; Bullard et al., 2007; Warren et al., 2007; Crouvi et al., 2012), enabling them to travel further through the atmosphere. Atmospheric loads become higher in clay content competency as the coarse mode particles settle out during emission and transport (Stuut and Prins, 2014; van der Does et al., 2018). Size fractions affect CCN and IN activation (Boose et al., 2016; Pöhlker et al., 2016; Amiri-Farahani et al., 2017), aerosol optical depth (Maher et al., 2010; Zhao et al., 2011; Kim et al., 2014; Kok et al., 2017; Alamirew et al., 2018), and solubility (Baker and Jickells, 2006; Journet et al., 2008; Ravelo-Pérez et al., 2016). Mineral and elemental composition of particles are a function of the parent rock (Scheuvens et al., 2013; Formenti et al., 2014b), soil mineralogy (Crouvi et al., 2012; Mileti et al., 2013), and source area climate (Evan et al., 2016; Williams et al., 2016). Aerosol composition is controlled by chemical and mechanical weathering processes that are climatically enhanced. Chemical reactions with rocks may include reduction and oxidation (Luther et al., 1982; Su et al., 2015; Preetz et al., 2017; Inda et al., 2018) or hydrolysis and solution (Schwertmann, 1985; Schwertmann, 1988; Long et al., 2016), while mechanical reactions may include aeolian abrasion and disaggregation (Bullard et al., 2007; Warren et al., 2007; Crouvi et al., 2012), hydration and dehydration (Schwertman, 1988; Dearing et al., 1996; Preetz et al., 2017), and leaching (Schwarz and Germann, 1999; Giorgis

et al., 2014; Long et al., 2016; Hettiarachchi et al., 2018). Mineralogy determines interactions with visible and invisible light spectrum, hygroscopicity, and gas and metal adsorption (Falkovich, 2004; Fang et al., 2017). Particle shape is a function of size and composition, thus also a function of the processes that control those aspects (Goudie and Watson, 1981; Crouvi et al., 2012). The roughness or smoothness of all grains is affected by abrasion via saltation, creep, and aeolian abrasion (Bullard et al., 2004; Bullard et al., 2007; Guan et al., 2016; Gherboudj et al., 2017; Ito and Kok, 2017), auto-abrasion by diatomite fragments (Bristow et al., 2005; Warren et al., 2007), and removal of grain surface coatings (Bullard and White, 2005; Bullard et al., 2007; Gherboudj et al., 2017). Frosting of quartz sand grains is facilitated by the chemical action of desert dew (Margolis and Krinsley, 1971). Smaller grains may also precipitate into definitive shapes such as cubes and bars (Coz et al., 2009; Coz et al., 2011; Matin et al., 2017). Grain roughness affects hygroscopicity (Levin et al., 1985; Semeniuk et al., 2007), refractive index (Levin et al., 1985; Kandler et al., 2007; Knippertz et al., 2007; Alamirew et al., 2018), and transport range of the grains (Formenti et al., 2011).

Study Area

Sahel Region

Between the Sahara Desert in North Africa and tropical Central Africa lies the Sahel transition zone, a 350 km wide belt that stretches from Mauritania and Senegal in the west to Sudan in the east (Fig. 1), from approximately 12*N to 20*N (OECD, 2010). Soil is a mixture of clay and sand that follows a north-south gradient, with more sand in the north and more clay in the south (Lopez et al., 2018). Vegetation in the Sahel is comprised of grassland, bushland, and some agricultural fields (OECD, 2010; Hereher, 2011; Cockerton et al., 2014; Thomas and Nigam, 2018). Rainfall is seasonal and follows the annual migration pattern of the Intertropical Convergence Zone (ITCZ)

over the Atlantic Ocean and continental North Africa (Fig. 2) (Lyons et al., 2010; OECD, 2010; Lopez et al., 2018). In late spring the ITCZ moves northward to around 15°N, bringing the West African Monsoon (WAM) to the Sahel (OECD, 2010; Lyons et al., 2012; Lopez et al., 2018). In July the rain belt moves southward to 5-10°N and the dry Harmattan winds blow from the northeast during the boreal fall and winter (Lyons et al., 2012; Lopez et al., 2018). Average annual rainfall in the Sahel is around 100 mm yr^{-1} in the north and 800 mm yr^{-1} in the south (Fig. 3) (Hereher, 2011). The Sahel has frequently undergone through decadal periods of drought in recent times, therefore it is known as a climate change "hot spot" due to its vulnerability to seasonal changes (OECD, 2010; Hereher, 2011).

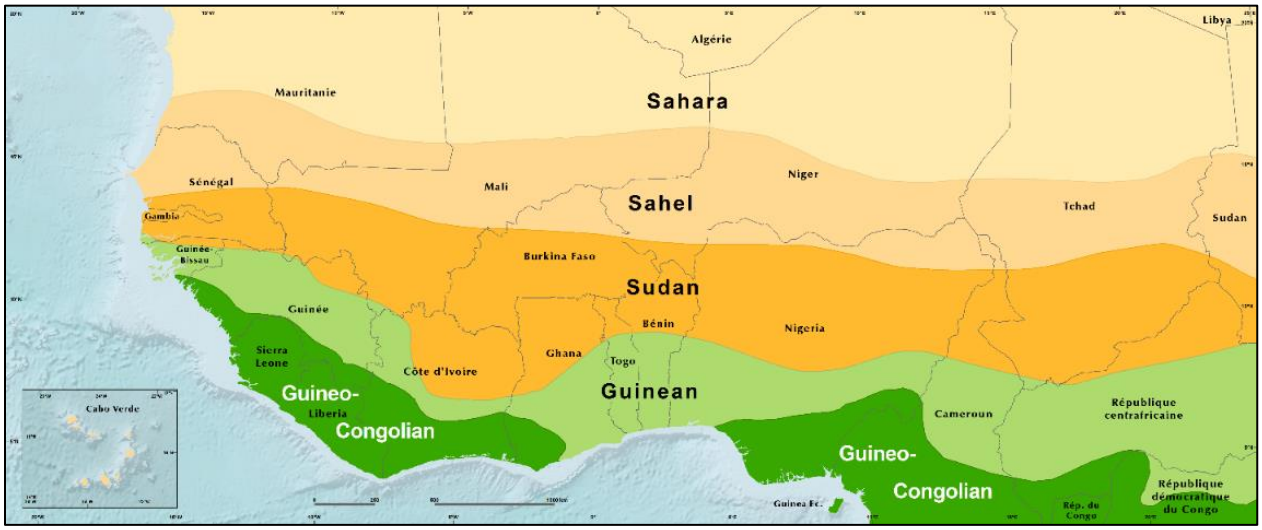

Figure 1. Climatic regions of North Africa (U.S. Geological Survey, n.d.)

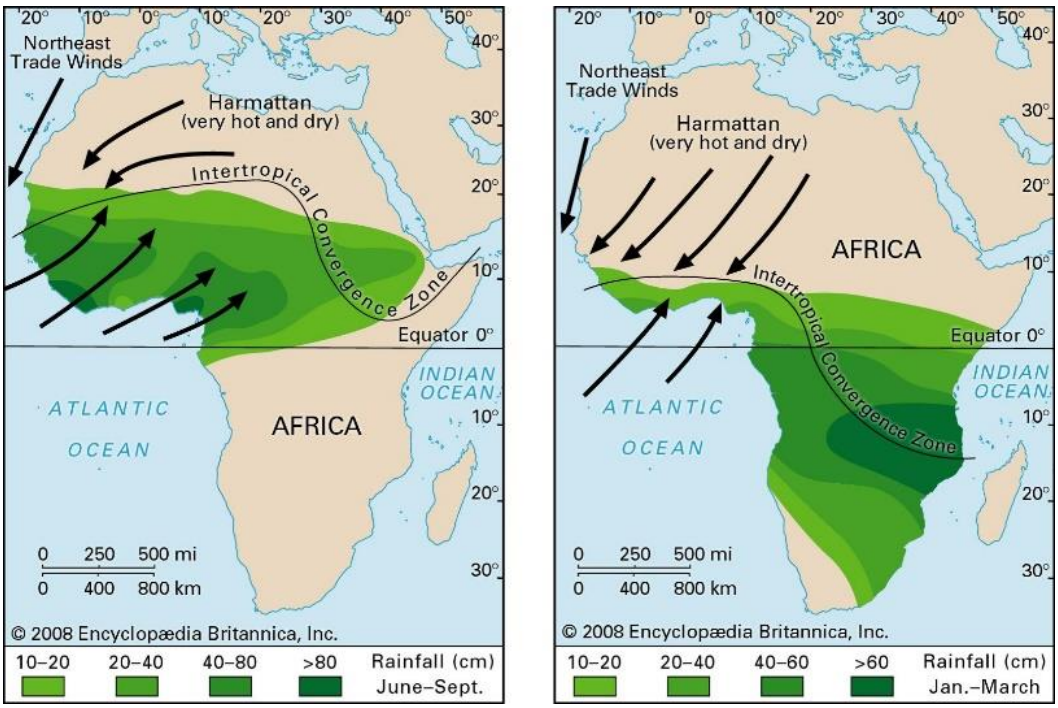

Figure 2. Location of ITCZ/tropical rain belt in boreal summer and winter (Encyclopædia Britannica, n.d.)

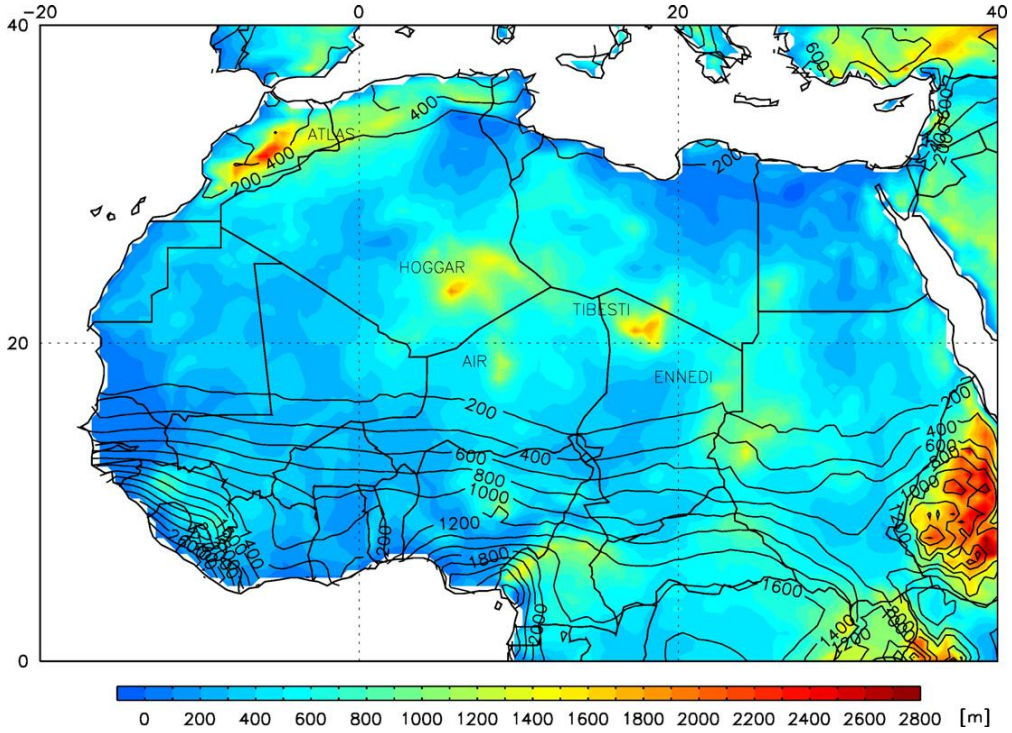

Figure 3. North Africa mean annual rainfall (Engelstaedter et al., 2006)

Saharan Metacraton

Chad and Niger are located on the Saharan Metacraton, a section of continental crust in north central Africa that partially mobilized and underwent metamorphosis during the Neoproterozoic Pan-African orogeny (Abdelsalam et al., 2002; Kröner and Stern, 2004; Shellnutt et al., 2017). Uplift of rocks created mountains including Precambrian Aïr Massif in northwestern Niger and Cenozoic Tibesti Massif in northern Chad and south Libya (Abdelsalam et al., 2002; Schuster et al., 2009; Shellnutt et al., 2017). The western boundary is the Raghane Shear Zone, roughly located at 8°30'E, that separates the metacraton from the Tuareg Shield. The eastern boundary is the Keraf-Kabus-Sekerr Suture that separates the Metacraton from the Arabian-Nubian Shield at 35°E. The southern boundary lies along the Benue Trough, Oubanguides Orogenic Belt and Aswa Shear Zone, roughly around 24°N, that separates the metacraton from the Congo Shield. The northern boundary is currently undefined, but is believed to lie under southern Libya and Egypt (Abdelsalam et al., 2002; Schuster et al., 2009). The bedrock consists of high-grade gneisses and migmatites (Abdelsalam et al., 2002; Kröner and Stern, 2004).

Chad Basin

The intracratonic Chad Basin is the largest endorheic basin in the world, covering an area over 2,500,000 km^2 over North Africa (Fig. 4) (Schuster et al., 2009; Bouchez et al., 2016). The basin is surrounded by mountainous regions – The Tibesti Mountains in the north, Air Mountains in the west, the Adamaoua region in the south and Ennedi Massif in the east (Bouchez et al., 2016). The depression contains lacustrine sediments that are mainly aeolian sands with increasing clay content (a variable mix of kaolinite and montmorillonite, with some illite) southward (Bouchez et al., 2016; Lopez et al., 2018). The sand flows from the northeast from Tibesti (Bouchette et al., 2010; Gherboudj et al., 2017). Seasonal rainfall in the basin follows the same trend as the Sahel. The south receives 700-800 mm yr^{-1} and the north receives 200-300 mm yr^{-1} (Bouchez et al., 2016;

Lopez et al., 2018). The Chad Basin is partitioned into two sub-basins, Lake Chad and the Bodélé Depression, a diatomaceous dry lakebed (Bristow et al., 2005; Armitage et al., 2015).

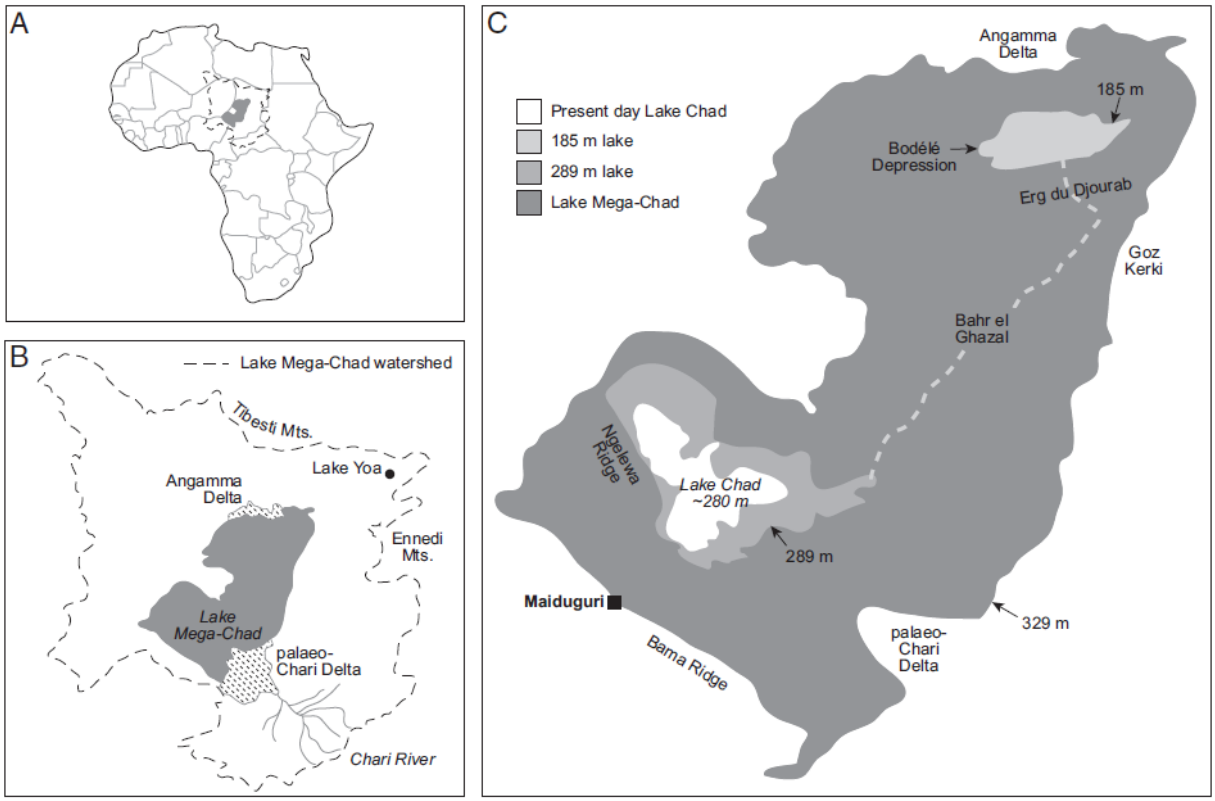

Figure 4. Locations of Lake Chad and paleolake Mega-Chad at highstand. (A) Location of Chad Basin in Africa. (B) Location of Paleolake Mega-Chad in the Chad Basin. (C) Location of Lake Chad within Lake Mega-Chad and highstand levels. If the level of Lake Chad exceeds 289 m it will flow through Bahr el Ghazal into the Bodélé Depression. (Armitage et al., 2015)

Lake Chad

Lake Chad is a freshwater lake that lies on the west-central edge of Chad (Fig. 4). The lake is large, but flat and shallow, only a few meters deep, so the surface area can fluctuate dramatically (Armitage et al., 2015; Bouchez et al., 2016; Bristow and Armitage, 2016; United Nations Environment Programme, 2018). In 1963 Lake Chad covered 26,000 km^2, but today it covers less than 1,500 km^2 (Schuster et al., 2009; Armitage et al., 2015; United Nations Environment Programme, 2018). The lake is fed from by the Chari and Logone Rivers flowing from the Central

African Republic and Cameroon (Schuster et al., 2009; Armitage et al., 2015; Bouchez et al., 2016) and outflow runs to the Bodélé depression via the Bahr el Ghazal dry riverbed (Drake and Bristow, 2006).

Bodélé Depression

The Bodélé Depression is a wind-deflated dry lakebed located in central Chad (Fig. 4), northeast of Lake Chad and south of the Tibesti Mountains (Bristow et al., 2005; Washington et al., 2006b; Schuster et al., 2009; Zhao et al., 2018). The Bodélé has been deemed the "dustiest place on Earth" because it is estimated that 64%±16% of all dust emissions from North Africa are emitted from the Bodélé (Bristow et al., 2005; Bristow et al., 2009; Schuster et al., 2009; Evan et al., 2014). The lakebed is comprised of easily erodible diatomaceous sediment overlying paleodune sand deposits and is nearly vegetation-free (Bristow et al., 2005; Washington et al., 2006b; Bristow et al., 2009). Northeasterly winds funneled between the Tibesti Mountains and Ennedi Massif, downslope winds, and radiatively induced turbulence create a low-level jet (LLJ) that scours the lakebed and releases diatomaceous dust plumes into the air (Washington et al., 2006a; Todd et al., 2007). The threshold for entrainment of particles is 10 m s^{-1}, and gusts in the Bodélé can reach up to 20 m s^{-1} in the winter (Bristow et al., 2005; Todd et al., 2007). Additional mesoscale convective systems and surface gusts contribute to the total dust emissions from the Bodélé (Engelstaedter and Washington, 2007; Schepanski et al., 2009; Kaly et al., 2015; Marticorena et al., 2017; van der Does et al., 2018).

Lake Mega-Chad

Lake Mega-Chad, a freshwater lake that was once the largest in Africa and filled a substantial portion of the Chad Basin (Fig. 4) (Schuster et al., 2009; Bouchette et al., 2010; Cockerton et al., 2014; Armitage et al., 2015; Bristow and Armitage, 2016). At highstand, the lake potentially covered 361,000 km^2 and was 150 m at the deepest part (Schuster et al., 2009; Bouchette et al.,

2010). Mega-Chad covered a large portion of Chad, engulfing the areas of present-day Lake Chad and the Bodélé. The lake was fed from the Tibesti Mountains in the north (Cockerton et al., 2014). After the end of the Last Glacial Maximum (LGM), around 11,500 years ago the African Humid Period began, and Lake Mega-Chad filled rapidly (Armitage et al., 2015; Bristow and Armitage, 2016). The boundary of the lake experienced fluctuating levels of high and low stand conditions until around 1,000 years ago, when the lake became nearly completely desiccated. The only hydrologically active portion that remains is today's Lake Chad (Drake and Bristow, 2006; Armitage et al., 2015; Bristow and Armitage, 2016).

Generation, Transport, and Deposition

Over half of all atmospheric dust is generated in North Africa (Bristow et al., 2009; Schuster et al., 2009; Evan et al., 2014). Over 80% of that amount is emitted from the Sahara Desert, and the remaining dust comes from the Sahel (Kim et al., 2014). Up to 100 dust plumes are generated in North Africa each year, emitting approximately 1,497 Tg yr^{-1} of dust into the atmosphere (Washington et al., 2009; Kim et al., 2014). Aerosol emissions are seasonal, following the migration of the rain belt of the ITCZ (Marticorena et al., 2017). Dust generation is controlled by wind emissions, topography, and soil and surface conditions (Maher et al., 2010; Evan et al., 2016; Gherboudj et al., 2017). Plumes from North Africa are carried upward and outward, and particles are deposited into far-reaching oceanic and land basins (Boy and Wilcke, 2008; Prospero et al., 2014a).

Generally speaking, dust is created by the erosion of soils and sediments by wind erosion (Bullard et al., 2007; Gherboudj et al., 2017). Grains are mobilized when surface winds speeds reach the threshold friction velocity of 10 m/s (Ginoux et al., 2012; Evan et al., 2016; Gherboudj et al., 2017; Kim et al., 2017). Once in motion, particles are carried by the wind via three different

methods, depending on their diameter: grains > 500 µm will roll along the ground, or *creep*; those between 70 and 500 µm will undergo *saltation*, wherein they receive some lift and bounce along the ground; and particles between 20 and 70 µm will experience short-term *suspension*, while those smaller than 20 µm will become suspended long-term (Fig. 5) (Bullard et al., 2007; Maher et al., 2010; Gherboudj et al., 2017). Saltation is the primary method of dust emissions, as bouncing grains will potentially generate more dust whenever they come into contact with the ground surface or collide with other particles, a process known as *sandblasting* (Gherboudj et al., 2017). When a saltating grain hits the surface, depending on surface conditions and soil properties, further particles may be ejected into the air. (Bullard and White, 2005) Forceful impacts between grains may cause one or both to fracture or chip, creating smaller pieces that can be carried farther distances (Bullard et al., 2007).

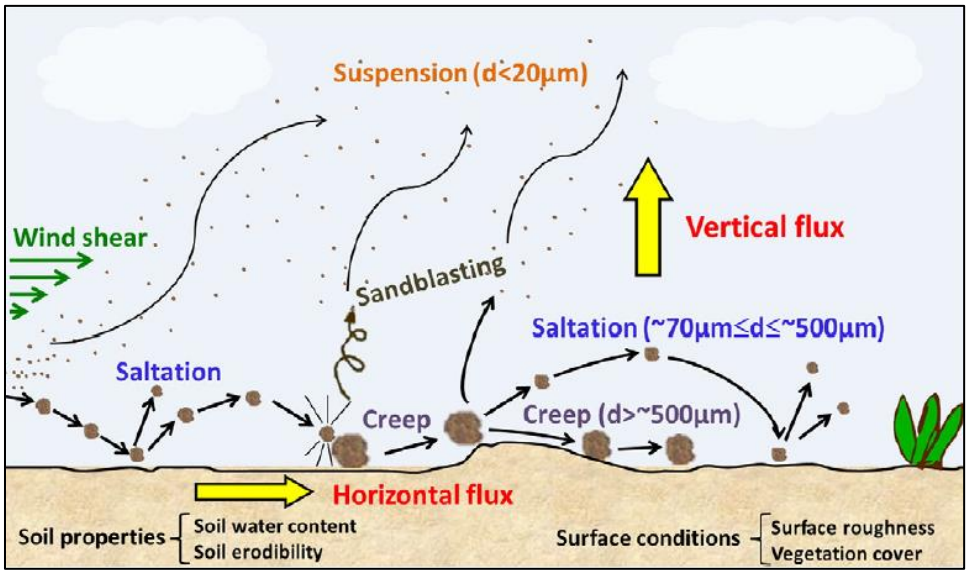

Figure 5. Dust mobilization processes (Gherboudj et al., 2017)

Wind

Wind conditions in source areas influence the amount of dust generated during an event. In the Bodélé, (winds experience diurnal changes (Engelstaedter et al., 2006). The dustiest part of the

day is mid-morning, when radiative heating creates turbulence and increases surface winds up to 13 m s^{-1} (Engelstaedter et al., 2006; Washington et al., 2006a; Washington et al., 2009). Average evening surface winds reach up to 6 m s^{-1}, generating very little dust (Washington et al., 2009). Mesoscale emissions events include dust storms called *haboobs* (Goudie, 2009; Schepanski et al., 2014; Kim et al., 2017), and microscale events include dust devils and dusty convective plumes (Engelstaedter and Washington, 2007; Knippertz et al., 2009; Kim et al., 2017). Seasonal winds in north central Africa are the northeasterly Harmattan winds between September and April, and the southwesterly WAM between May and August (Fig. 6) (Lyons et al., 2010). During the summer, in the latitudes above the Sahel storm belt, the Harmattan and trade winds converge over the Sahara (Engelstaedter et al., 2006). The result is strong turbulence, increased surface winds, and large-scale dust storms (Engelstaedter et al., 2006). Peak dust emissions from North Africa occur during the dry winter, when the ITCZ has moved to lower latitudes (Gherboudj et al., 2017).

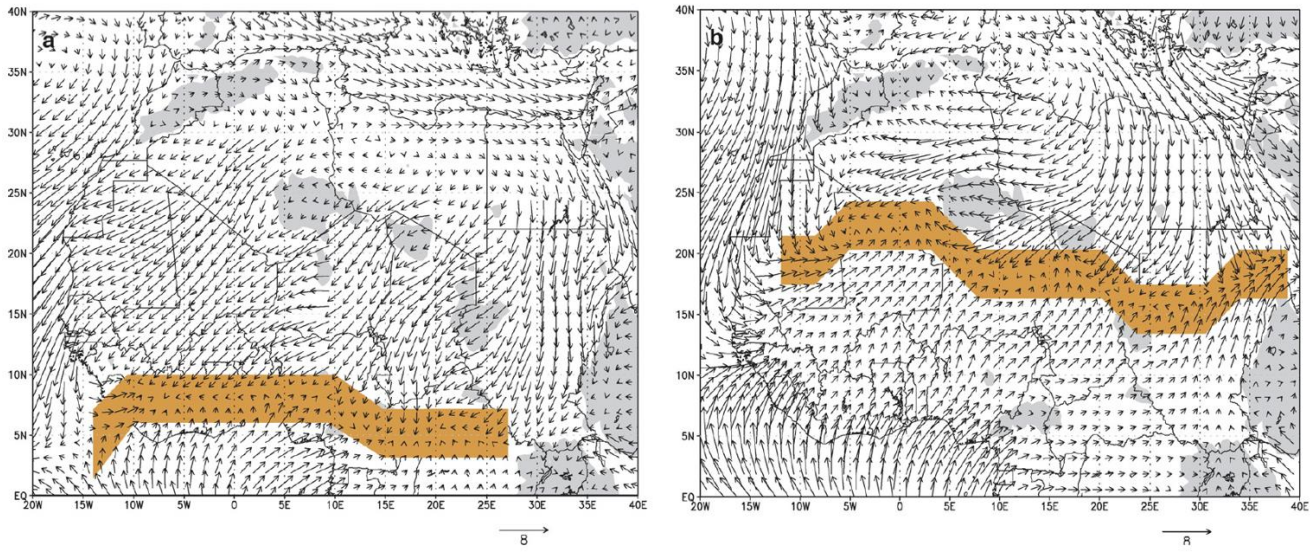

Figure 6. Mean surface wind speed in m/s over North Africa for (a) winter and (b) summer. Longer arrows denote faster winds. Topographic highs are shaded grey. Converging wind belts are in orange. (Engelstaedter et al., 2006)

Figure 7. Locations of dust and sediment samples. Arrows denote the direction of the Harmattan winds between Tibesti Mountains and Ennedi Massif (Google Maps, 2019).

Topography

Topography plays an important role in dust emissions by disrupting wind trajectories and creating convective disturbances (Schepanski et al., 2009). Hot spots for dust emissions include flood plains, depressions, wadis, arroyos, and alluvial fans (Goudie, 2008; Crouvi et al., 2012; Ginoux et al., 2012; Gherboudj et al., 2017). Mountains produce clouds, lee cyclones, and downslope forcing that can increase surface winds by up to 40% (Todd et al., 2007; Schepanski et al., 2009; Washington et al., 2009). Maximum wind speeds occur downwind from gaps between mountains (Engelstaedter and Washington, 2007; Knippertz and Todd, 2010; Evan et al., 2016). For example, when the Harmattan winds blow between the Tibesti Mountains and Ennedi Massif they create a *Venturi effect*, wherein static pressure decreases and wind velocity increases (Fig. 7) (Ginoux et

al., 2012). When combined with downslope winds from Tibesti and Ennedi, a LLJ is created that blasts the dry lake bed of the Bodélé Depression and creates massive dust storms (Todd et al., 2007; Warren et al., 2007; Schepanski et al., 2009; Washington et al., 2009). LLJs occur in all months of the year except August, and the peak occurs in the winter when the Sahel is dry (Washington and Todd, 2005; Engelstaedter and Washington, 2007; Warren et al., 2007). The dustiest years on record have been attributed to years with strong LLJs (Washington and Todd, 2005; Warren et al., 2007).

Soil and surface conditions

Soil properties and surface conditions can affect several aspects of dust emissions and surface deflation in highly erodible regions such as the Bodélé Depression (Ginoux et al., 2012; Gherboudj et al., 2017). Soil moisture from rain and dew reduces increases the threshold wind friction velocity and promotes particle aggregation, thus suppressing dust emissions (Mahowald et al., 2006; Ito and Kok, 2017; Lopez et al., 2018). Desiccation cracks in dry pavements stimulate discharges by allowing more surface area for air convection and wind erosion (Lopez et al., 2018). Finer surface materials such as silt and clay are highly susceptible to wind erosion (Goudie, 2008; Armitage et al., 2015; Gherboudj et al., 2017). Sandblasting in the Bodélé has been very effective at propagating dust emissions due to the ease of deflation of the fine diatomaceous sediments (Washington et al., 2006b; Bristow et al., 2009). Rougher soils create more friction, increase the threshold friction velocity, and lower dust flux (Menut et al., 2013; Ito and Kok, 2017). Vegetative cover indirectly affects dust emissions by reducing surface wind speed and increasing soil moisture content (Tegen et al., 2004; Cowie et al., 2013; Ridley et al., 2014; Kim et al., 2017). Land use changes caused by agriculture and encroachment of forests only contribute <10% of the North African dust flux (Tegen et al., 2004; Kuhnert et al., 2010). However, indirect anthropogenic

influence on emissions will be in the form of climate change and its effects on desertification (Tegen et al., 2004; Ridley et al., 2014).

Transport

Dust plumes from the Sahara and Sahel distribute horizontally and vertically over large areas in a short amount of time (Husar, 2004; Gross et al., 2016). Increased wind speed and temperature drops brought on by downslope winds promote convection (Knippertz et al., 2007). Density currents create turbulent winds that carry particles to higher altitudes (Knippertz et al., 2007). Markers for source regions can be diluted within one to two days as plumes mix with the dense marine layer and free troposphere (Formenti et al., 2014b; Patey et al., 2015). In the marine layer, particles commingle with sea spray and pollution (Denjean et al., 2016). In the free troposphere lies a hot, dry corridor called the Saharan Air Layer that extends from North Africa to the Americas (Dunion and Velden, 2004; Boose et al., 2016; Denjean et al., 2016; Ravelo-Pérez et al., 2016; García et al., 2017). Particles travel farther and faster in the SAL due to the higher wind speeds (Husar, 2004). Over 90% of the total mass of the SAL is dust (García et al., 2017). The dust column may be well-mixed or stratified by different plumes and particle shapes (Denjean et al., 2016). Due to wind resistance, grains are sorted by altitude based on their roundness, with the most aspherical particles at the top of the column (Yang et al., 2013). Strong turbulence can keep coarse particles in suspension for several days. During the boreal summer, strong winds and turbulence in the SAL can carry angular particles >100 μm to remote regions of the Atlantic Ocean (Mahowald et al., 2005; van der Does et al., 2018).

Deposition

Once entrained, dust is removed from the atmospheric overburden by dry or wet deposition. The majority of the dry deposition takes place in the form of gravitational and shape-induced settling (Kim et al., 2014). There is more dry deposition near the source, particularly when dust

concentration is high (Marticorena et al., 2017; Middleton, 2017). Wet deposition is primarily linked to cloud scavenging, when particles within clouds act as CCN or IN, and particles below clouds connect with falling water droplets (Kim et al., 2014; Marticorena et al., 2017). Wet deposition is the primary method over the ocean (Engelstaedter et al., 2006). Over the Sahel, peak deposition occurs just after peak dust emissions, but before the height of the rainy season (Marticorena et al., 2017). The average flux in the Sahel is 75 to 183 g m^{-2} yr^{-1} (Marticorena et al., 2017).

In the North Atlantic, North African dust has deposited important nutrients including iron (Jickells et al., 2005; Waeles et al., 2007; Mendez et al., 2010; Powell et al., 2015), phosphorus (Mills et al., 2004; Mather et al., 2008; Gross et al., 2016), and nitrogen (Jickells et al., 2016). Aerosols over the ocean are also enriched in trace metals including titanium, manganese, vanadium, cobalt, and thorium (Jickells et al., 2016). Saharan dust outbreaks can travel north to the Mediterranean and the Iberian Peninsula (Pérez et al., 2008; Pulido-Villena et al., 2008; Coz et al., 2009; Querol et al., 2009). During the boreal summer, dust follows a northern path to southeastern United States and the Caribbean (Yu et al., 2015a). Aerosols contribute to phytoplankton growth and soil fertility in Barbados and the Bahamas (Muhs et al., 2007; Prospero et al., 2014b; Chien et al., 2016; Williams et al., 2016), asthma in Grenada and Puerto Rico (Akpinar-Elci et al., 2015; Ortiz-Martínez et al., 2015), and red tides in Florida and the Gulf of Mexico (Walsh et al., 2006; Lenes et al., 2008). In the winter and spring, the flow moves southward, bringing coarse mode pulses into French Guiana and the Amazon Basin (Prospero et al., 1981; Prospero et al., 2014a; Yu et al., 2015b). Dry spells during La Niña years have brought dust as far west as the Andean rain forests in Ecuador (Boy and Wilcke, 2008).

It is evident that the Sahel is an important environmental system with a complicated pedogenic environment. The purpose of this study is to (1) investigate the use of Munsell soil color analysis as an indicator of the intensity of weathering, (2) identify physical characteristics of magnetic heavy metals on an individual basis using SEM, (3) identify the chemistry of the magnetic particles using EDS, (4) relate the characteristics of natural particles to the weathering conditions in the climate-sensitive Sahel corridor, and (5) identify any contaminants in the samples.

The common magnetic iron oxide minerals in the environment vary in their degree of response to a magnetic field. Strongly magnetic minerals such as magnetite (Fe_3O_4) and maghemite (γFe_2O_3) are referred to as ferrimagnets. The antiferromagnets such as ulvospinel (Fe_2TiO_2), ilmenite ($FeTiO_2$), and the iron oxyhydroxide goethite ($\alpha FeOOH$) plus the canted-antiferromagnets such as hematite (αFe_2O_3), exhibit weaker magnetic properties.

Methods

Eight samples were chosen out of a pool of 57 dust and surface sediment samples collected from the Sahel in September 2010. Samples had been stored in a temperature-controlled laboratory in plastic zipper bags. The chosen locations follow a west-east transect through southeastern Niger and central Chad (Fig. 7, Table 1). Samples chosen from the pool are unsorted mixes of dust and surface sediments.

Table 1. Locations and types of samples

Site number	Type of sample	Latitude (North)	Longitude (West)	Elevation (masl)
18	Dust	13°52.681	10°24.874	389
21	Surface sediment	13°31.692	11°45.922	336
24	Surface sediment	13°26.963	12°47.457	312
28	Surface sediment	14°24.738	13°36.690	283
30	Dust	13°53.765	14°14.806	290
35	Surface sediment	13°43.987	16°00.431	289
36	Surface sediment	13°38.924	16°29.385	288
40	Arid sediment	14°56.899	17°22.992	279

Roughly 0.18 g of samples were placed in separate test tubes, each with 0.02 g of liquid surfactant and DI water. Test tubes were placed in a sonicator for 30-60 minutes to disaggregate the particles. Disaggregated solutions were placed in a large petri dish and swirled over a neodymium-iron super-magnet to separate the magnetic particles from the mixture (Fig. 8). A pipette was used to transfer the strongly magnetic fraction from the petri dish to a glass slide. The slide was covered

and left to dry overnight. The dried magnetic particles were then affixed to a stub with double sided carbon tape, which was then evaporatively coated with thin carbon layer.

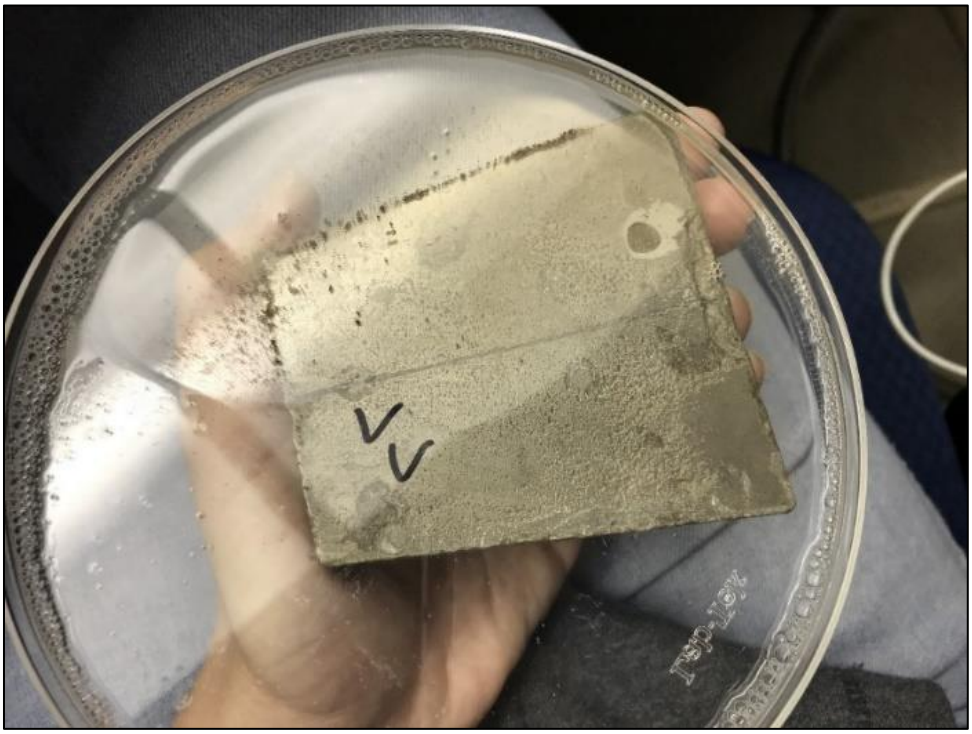

Figure 8. Magnetic particle separation with neodymium magnet

Backscatter and secondary imaging were performed on FEI/ASPEX [PSEM] with Perception (proprietary) software. Additional secondary imaging was performed at 20 kV with Zeiss Supra 55VP Field Emission Scanning Electron Microscope and SmartSEM software. Chemistry analysis was performed with energy-dispersive X-ray spectroscopy, performed with Bruker XFlash 6160 ES Detector and Quantax Esprit microanalysis software.

It has been determined that hematite in tropical soil will give red to black values, while goethite will give the soil yellow to brown values (Hurst, 1977; Camêlo et al., 2017). In 1977, Hurst suggested the use of Munsell soil colors to estimate the quantity of hematite to goethite in saprolite, as the hue of pure hematite is 7.5R and the hue of pure goethite is 10YR (Torrent et al., 1980), and

most soils that contain hematite will register at least 5YR (Liu et al., 2016; Preetz et al., 2017). Hurst (1977) used the formula H*L/C, where H* is the absolute value of the hue, L is the lightness (also known as value), and C is the chroma and plotted them on a log plot (Fig. 9).

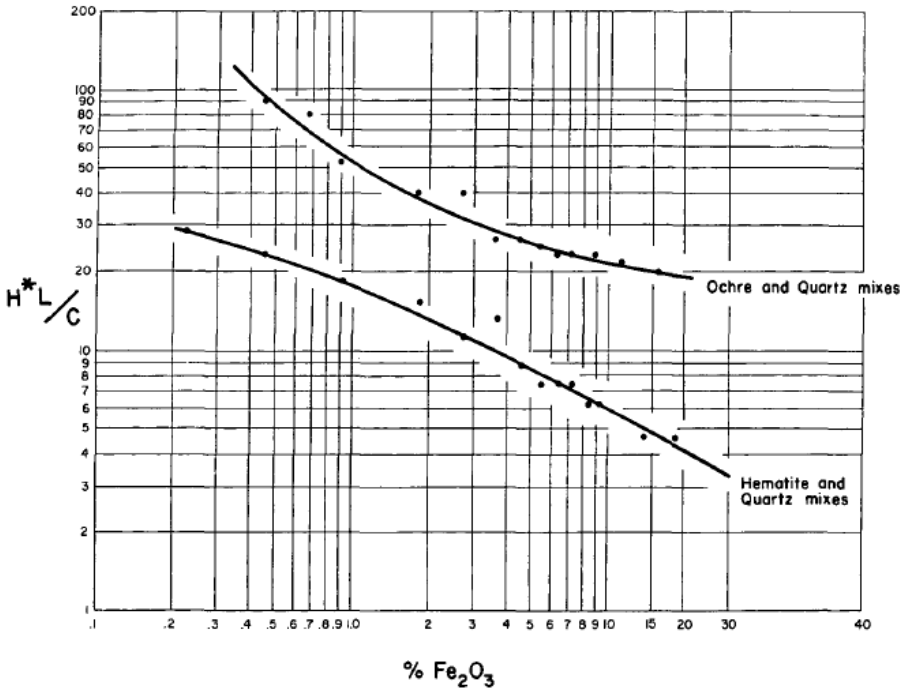

Figure 9. Hematite-goethite ratio log plot from Hurst (1977).

Visible-based characterization of sediment redness was performed using a Munsell color chart (Munsell Color, 1998) under fluorescent lighting, but next to a window with natural light (Fig. 10). Two analysts determined each color. Hurst's (1977) original calculation of H*C/L was used, and the two calculations of each sample were averaged together, as suggested by Preetz et al. (2017).

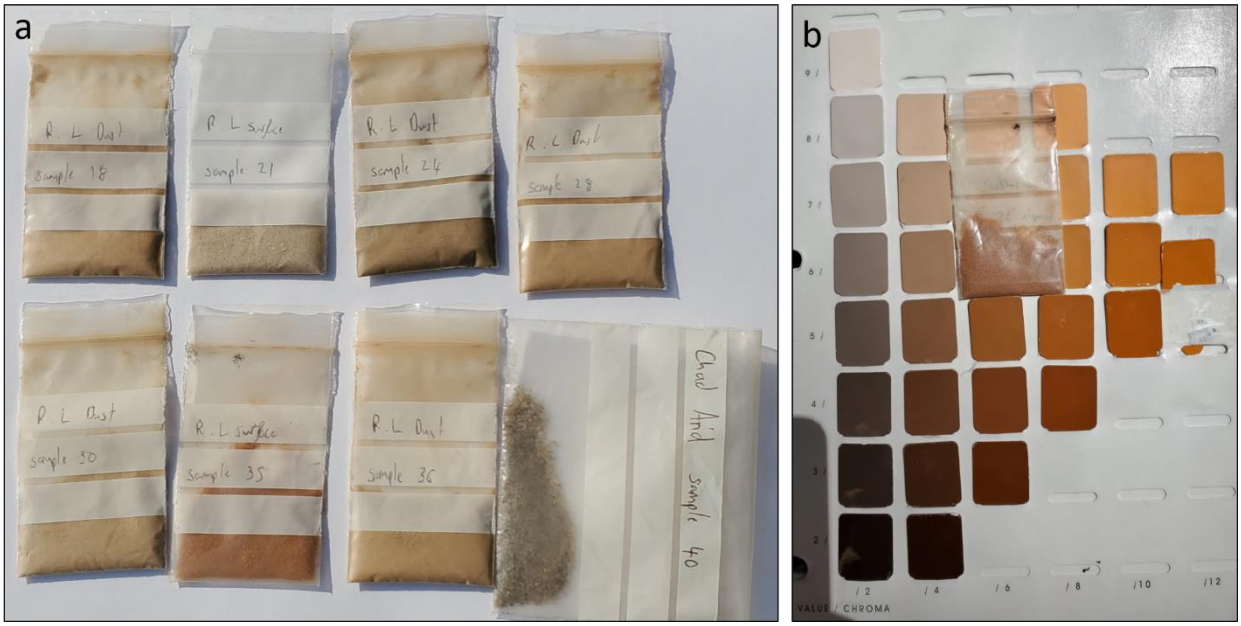

Figure 10. Munsell soil color analysis; a) dust samples in plastic zipper bags; b) color matching with Munsell book.

Results

Munsell soil color analysis

Table 2. Results of soil color analysis.

Sample	Analyst 1					Analyst 2					Average
	Color	H*	L	C	H*L/C	Color	H*	L	C	H*L/C	H*L/C
18	10YR 7/4	20	7	4	35	10YR 7/4	20	7	4	35	35
21	2.5Y 8/2	N/A	8	2	N/A	10YR 8/2	20	8	2	80	N/A
24	10YR 6/4	20	6	4	30	10YR 7/2	20	7	2	70	50
28	10YR 7/4	20	7	4	35	10YR 6/4	20	6	4	30	32.5
30	2.5Y 8/4	N/A	8	4	N/A	10YR 7/4	20	7	4	35	N/A
35	7.5YR 6/6	17.5	6	6	17.5	7.5YR 5/4	17.5	5	4	21.9	19.7
36	10YR 7/4	20	7	4	35	10YR 7/4	20	7	4	35	35
40	2.5Y 5/2	N/A	5	2	N/A	2.5Y	N/A	5	2	N/A	N/A

Munsell soil color analysis was conducted independently by two individuals. The results are listed in Table 2. Only two of the samples were assigned the same color by both analysts - 18 and 36. The H*L/C results for samples from both analysts were averaged together for the actual H*L/C, as performed by Preetz et al. (2017). Three of the samples (21, 30, and 40) were deemed outside of the color range to be considered for Munsell analysis by analyst 1, and one sample (40) was outside the range for analyst 2.

SEM and EDS

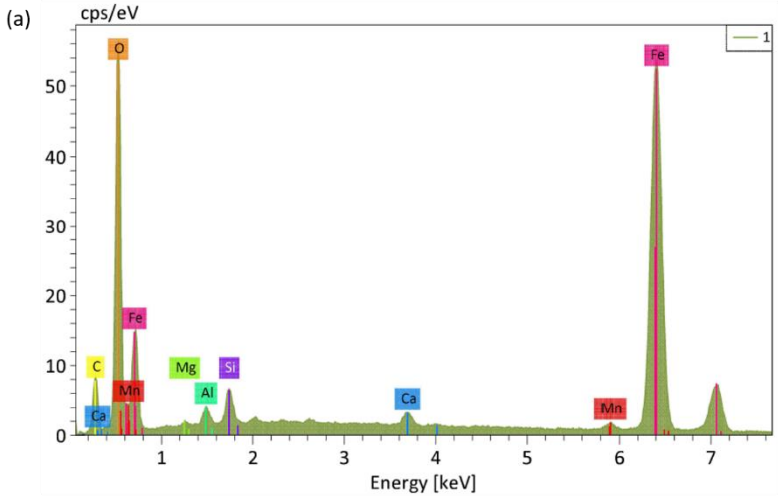

(b)

Element	At. No.	Netto	Mass [%]	Mass Norm. [%]	Atom [%]	abs. error [%] (1 sigma)	rel. error [%] (1 sigma)
Iron	26	135474	55.58	55.25	25.18	1.50	2.71
Oxygen	8	55999	31.62	31.43	50.00	3.72	11.77
Carbon	6	7186	10.90	10.84	22.97	1.63	14.95
Silicon	14	5932	0.84	0.83	0.75	0.06	7.63
Calcium	20	3825	0.72	0.71	0.45	0.05	6.97
Manganese	25	1554	0.49	0.49	0.23	0.04	8.94
Aluminium	13	2227	0.45	0.45	0.42	0.05	11.26
Magnesium	12	0	0.00	0.00	0.00	0.00	3.46
		Sum	100.60	100.00	100.00		

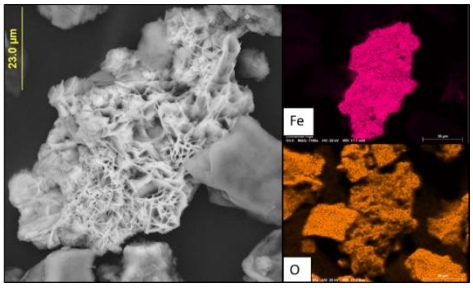

Figure 11. SEM and EDS results: (a) X-ray spectrum of a particle, (b) quantitative results in mass % of elements, (c) SEM image and EDS relative proportion maps. Elements with <1% of the total mass were excluded from final maps. Carbon results were removed because they would be masked by the carbon coating.

Figure 11 shows a typical output for particles examined using SEM and EDS. The y-axis of the x-ray spectrum (at top) is a record of the number of X-rays generated by the interaction of the primary electron beam with the sample. The x-axis records the energies of the characteristic X-rays (each element generates X-rays with specific energies when the primary electron beam interacts with the sample) that provide compositional information on the sample (Ryan, 2014). Plates of the SEM images and maps of all particles examined are found in the Appendix. Elements that contributed <1% to the total mass were removed from consideration. EDS analysis does not provide definitive insight into specific minerals when the elemental constituents are the same. Therefore, minerals

high in iron and oxygen (hematite (Fe_2O_3), maghemite (γFe_2O_3), and goethite (FeOOH)) are classified under a general iron oxide category. Grains with high quantities of iron, titanium, and oxygen are classified as iron-titanium oxides. Particles with very high titanium constituents without a strong iron component are titanium dioxides. All other particles were grouped as mine wastes and unclassified technogenic magnetic particles (TMPs).

Iron oxides (Plates 1-8)

Iron oxide precipitates can take many forms, such as bulbous botryoids, acicular needles, or platy grains (Mindat, n.d.) (Plate 1). Precipitation as secondary minerals can begin as micro-sized grains or spherules (Plates 2-3). Iron oxides may also precipitate amorphously (Plate 4), or be present as part of iron-rich clay coatings that can chip when subjected to abrasion, creating smaller, angular grains (Plate 5) (Bullard et al., 2007). As grains undergoing dissolution diminish in size, they provide more surface area for further chemical weathering reactions (Plate 6) (Baker and Jickells, 2006). Grains containing pieces of diatoms likely originated from the Bodélé (Engelstaedter et al., 2006; Moreno et al., 2006) (Plate 7a). Several grains exhibit evidence of both dissolution and precipitation of secondary minerals (Plates 2b, 3, 7b, 8). The shrinkage cracks exhibited in Plate 7b are indicative of maghemitization (Merrill, 1975).

Fe-Ti oxides (Plates 9-12)

The Fe-Ti oxides (titanomagnetites and ilmenite) found in this study area exhibited less amorphous and more crystalline characteristics, such as the barrel and rhomb (common with ilmenite) habits in Plate 9. Well-rounded particles may reflect some chipping and spalling (i.e. breaking or fragmenting) (Plate 10). Euhedral zircons were found throughout the samples (Plate 10c), and left

casts in some of the Fe-Ti oxides (Plate 11). Zircon casts were not found in any of the other mineral classifications. Fe-Ti oxide dissolution features are shown in Plates 11 and 12.

Some grains exhibited dissolution and precipitation features that are not easily attributed to one process (Plates 12b and c). The particles are striated, and on closer magnification showed nodular and needle-like precipitations. One interpretation is that these are ore deposit grains that weathered *in situ* or in gaps between plates of clay. The grains may have undergone sandblasting in one direction while still attached to a rock, giving them a striated effect before they were dislodged. The grains may then have been undergone additional precipitation, leading to the nodules seen in the closeup picture of 12c. Another possible explanation is that this is a TMP, and a coating has developed over it. There may be another explanation for these features, however, it is evident that the particles have had a complicated history that is unexplained by just one set of conditions.

Titanium dioxides (Plates 13-14)

Only three particles from the dust samples were identified as TiO_2. Plate 13 shows a near-perfect example of reticulated rutile. It is likely that the entire grain was once the "log cabin-style" stacking rutile structure seen in Figure 12 (Force et al., 1996). The gaps appear to have been filled with a clay cement and the grain has been rounded out by tumbling through the environment. The grain in 14a shows distinct precipitation of spherules that have either formed entirely into the angular grain shape, or has created a very thick coating over another particle. 14b appears to be a TiO_2 particle that has undergone dissolution, but retained its original outer structure. It is possible that the structure of the particle is a TMP that has developed a Ti-dioxide coating.

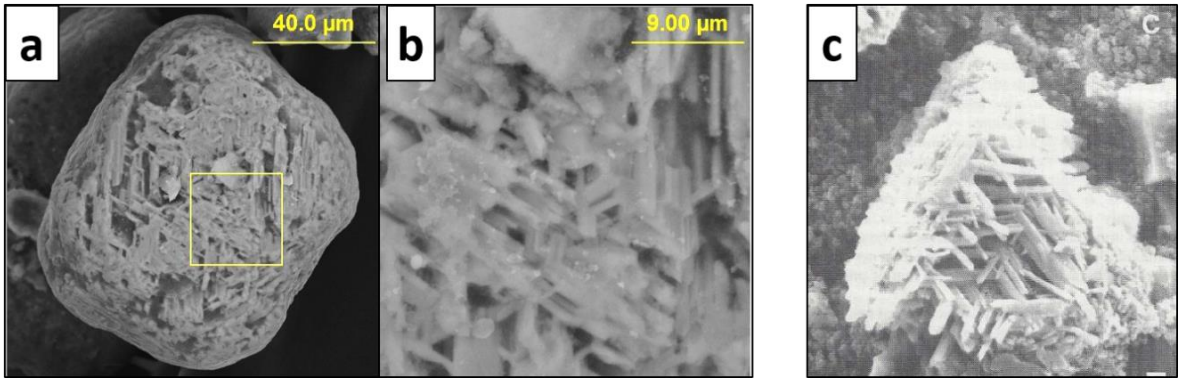

Figure 12. Titanium dioxide structure (a and b) particle from sample 21, (c) "log cabin-style" stacking from Force (1996)

Other heavy metals and unclassified technogenic magnetic particles (Plates 14-17)

Particles containing toxic heavy metals and without a strong iron or titanium component were found in five of the eight samples. Some of the grains are considered to be TMPs. TMPs are magnetic particles of anthropogenic origin that have undergone high-temperature processing, such as metallurgy, fuel combustion, and cement manufacturing (Bourliva et al., 2017). The Sahelian samples were collected roadside, but evidence exists for the particles to have originated from cement production or mine waste. Particles were thus split into two groups – mine waste and unclassified TMPs. Particles containing elements naturally found in regional mining areas, barium and cerium, were considered to come from the mines. A pyrite (FeS_2) framboid was placed in the mining category as a byproduct of excess sulfate and iron in the mine waste. The other particles are considered unclassified TMPs, as their source could not be ascertained without further chemical analysis.

Discussion

Munsell soil color analysis

The ratio of hematite to goethite in soils is an important climatic and environmental indicator. These two iron oxides form as secondary minerals from ferrihydrite, and dominance is obtained based on factors including pH, soil moisture, and content of other elements in the soil (Jiang et al., 2016). In general, acidic or alkaline soils developed in humid areas will obtain higher quantities of goethite, and hot, arid areas with soils high in Al will have higher quantities of hematite (Torrent et al., 1980; Jiang et al., 2016; Camêlo et al., 2017). Hurst (1977) developed a method to assess the ratio of goethite to hematite in the field using a Munsell soil color chart. Soil rubefaction is accounted for by using the hues of 5YR to 10R, because soil colors that are higher in hematite than goethite generally fall within the yellow-red to red spectrum (Hurst, 1977; Torrent et al., 1980; Preetz et al., 2017). Increasing redness rating (H*L/C) indicates an increase in hematite compared to goethite (Hurst, 1977). Since goethitic soils are generally yellow and depleted in hematite, hues in the yellow (2.5Y to 10Y) range are not applicable for the Munsell method (Camêlo et al., 2017).

Calculating the redness rating is not a precise method for quantifying hematite and goethite in a sample, as numerous factors can affect the color (Bullard and White, 2002). Iron-rich coatings will chip away from particles as they are abraded by sandblasting (Bullard et al., 2004). The darker fine-grained chips will be transported further from their source. Therefore, the precise amount of hematite will be lost in unsorted sediment mixtures, particularly with increasing distance from the source (Bullard et al., 2007). Wet soils will reflect a lower lightness and may increase the chroma (Hurst, 1977). Soils containing other minerals such as manganese hydroxides will lower the lightness (Hurst, 1977). Color selection is subjective and can vary from person to person and between different parent material, as shown in the results of this experiment (Table 2) (Preetz et

al., 2017). Hurst (1977) found that using a visual assessment of the redness rating compared to the true contents of his soils was only accurate within 15%. Bullard and White (2002) used visible reflectance spectrometry in the field and compared results with a Munsell color book, using Torrent's (1980) calculations. Results were comparable between both methods; however, the spectrometry was more precise. Therefore, use of the Munsell visual estimation method will only provide a general analysis for degree of weathering in the field, when precision is not necessary (Bullard and White, 2002). Color test records may be useful in areas that are transitional between arid to tropical, such as the Sahel, to determine changes in weathering between them.

The redness rating for the samples are listed in Table 2. No trend in rubefaction was found among the samples. Null values were interspersed with low to mid-range values. Sample 40 received a null value from both analysts, likely because of its close proximity to the Bodélé. The sediment was yellow-grey and expected to be high in diatomaceous grains, making it unsuitable for the Hurst method. The average redness rating cannot be calculated for samples 21 and 30 because one of the two analysts determined their hues as 2.5Y. The fact that these soils that straddle the line between red and yellow are important, as they mark the division between hematite and goethite weathering regimes. Using visible reflectance spectrometry on the complete suite of samples available may reveal a more definitive pattern in hematite to goethite ratios and weathering regimes (Bullard and White, 2002).

SEM and EDS

Multiple studies have determined that over 90% of the composition of mineral dust and sediments of North Africa is primarily clays, quartz sand, Fe oxides, and Ti dioxides (Moreno et al., 2006; Chou et al., 2008; Scheuvens et al., 2013; Formenti et al., 2014a; Gross et al., 2016; Rocha-Lima et al., 2018). Magnetite and titanomagnetite are common in rock types from ultrabasic to

intermediate, and are therefore common in the dusts and sediments of North Africa (Preetz et al., 2017). Harmattan winds blow sediments into the Chad Basin from eroded Pan-African orogenic rocks of the Tibesti Mountains, Egypt, and Sudan, carrying minerals that include kaolinite, hematite, goethite, anatase, and rutile (Schwarz and Germann, 1999; Sokolik and Toon, 1999). The natural minerals identified in assessment reflect the expected physicochemistry of the dusts and sediments in the Sahelian Chad Basin study area. The remaining particles identified are contamination that may have come from mining, cement processing, or transportation (Pagotto et al., 2001; Plumlee and Ziegler, 2007)

Over half of the mass of Fe in North African mineral dust is present as iron oxides including hematite, goethite, and magnetite (Formenti et al., 2014b). Dry conditions will promote hematite formation, and areas that undergo seasonal wetting and drying may have particles that exhibit both dissolution and precipitation of secondary, fine-grained minerals on the same grain (Lyons et al., 2010; Gao et al., 2018). Precipitation onto grains may create aggregates that include foreign particles such as *Aulacoseira* diatoms (Engelstaedter et al., 2006; Moreno et al., 2006).

Titanium is commonly found as a substitution element in clays, and the Bodélé is enriched in titanium (Dolcater et al., 1970; Scheuvens et al., 2013). Titanium and iron can often be found together in nature in varying mixtures in the same minerals, and both can be removed from their constituents by similar processes (McLaughlin, 1954). Heavy iron-titanium minerals such as ilmenite are preferentially in the coarse fraction, and require high winds to travel farther distances (Grousset et al., 1998).

Titanium dioxides (rutile and anatase) account for 1% of mineral dust mass in the Sahara Desert and 2% of mineral dust mass in the Sahel in both the coarse and fine fraction (Chou et al., 2008; Formenti et al., 2014b). TiO_2 has catalytic properties that enable it take part in important

photochemical reactions (Ndour et al., 2008). For example, Ti dioxides in Saharan dust events can act as a radical and potentially reduce atmospheric NO_2 levels by 37% and atmospheric ozone by 5% (Ndour et al., 2008).

It would be difficult to pinpoint where the other heavy metals and TMPs in the samples originated. Scheuvens et al. (2013) suggest that any lead inputs to African dust are due, at least in part, to anthropogenic inputs. For example, road traffic emits lead, zinc, copper, and chromium TMPs into the air daily (Pagotto et al., 2001). Additionally, vehicles and ordinance remain in the Bodélé from the 1980s Cold War (Fig. 13) (Washington, 2006c). It is likely that regular erosion from the Harmattan winds distributes pieces of metal from these sources into the air. Cement production emits into the atmosphere gases and dust rich in heavy metals and metal sulfides, commonly nickel, zinc, and lead, with some chromium possible (Trezza M. A. and Scian A. N., 2007; Estokova et al., 2018; Arfala et al., 2018). The source of lead-zinc minerals is also likely to have originated in the Benue Trough, a rift system along the eastern border of Nigeria that leads into the Chad Basin (Ola-Buraimo and Abdulganiyu, 2017). The trough consists of claystones, shales, sandstones, and limestones that contain hydrothermal deposits of barite ($BaSO_4$), galena (PbS), and sphalerite (ZnS) (Fatoye F. B. et al., 2014). The deposits extend the length of the trough, which has undergone small-scale mining activities (Fatoye F. B. et al., 2014). Uncontrolled mining emit byproducts of lead, zinc, copper, chromium, and nickel that are discharged into the air and waterways (Ayres, 1992; Fashola et al., 2016; Masindi and Muedi, 2018). Due to the high amounts of barite found in the Benue trough, samples with a barium component are considered to be from the mines. Pyrite (FeS_2) framboids, such as the one seen in Plate 14c, are found in anoxic environments where sediment is rapidly deposited, where bacteria can reduce sulfate into H_2S. The framboid was found in sample 40, the closest to the Bodélé, and the most unlikely environment for it the grain to

precipitate (Farrand, 1970; Roberts and Turner, 1993). The various metal sulfides and metal sulfates found in mine drainage are a likely source of the sulfur for the pyrite framboid (Plumlee and Ziegler, 2007).

Figure 13. Vehicles and ordinance from the Bodélé (Washington, 2006c).

In the month prior to the collection of these samples, North Africa encountered its strongest monsoon season in 80 years (BBC News, 2010; Quist-Arcton, 2010; Mahecic, 2010; Al Jazeera, 2010). 80 km to the south of Lake Chad, N'Djamena, the capitol of Chad, experienced widespread flooding (IRIN, 2010). It is speculated that mine waste from Nigeria or Sudan flowed into the Yobe, Logone, or Chari rivers and was carried to the basin in floodwater. Niger has experienced more massive flooding events in 2012 (IRIN, 2012a; IRIN, 2012b) and 2017 (Le Cam, 2017). As the Sahel warms, more moisture is retained in the atmosphere, bringing more rain to the area (Le Cam, 2017). Further studies may want to focus on anthropogenic contamination in areas that are at a high risk of inundation of mine waste.

The presence of zircons among the Fe-Ti oxides (Plates 10c and 11) may be helpful in future geochronology studies. Radiogenic uranium and thorium are often found naturally in zircons, making them excellent for use in rock age dating (Ryan, 2014). Zircon is common among igneous rocks, and the samples were full of them (Churchman et al., 2012). Isotopic measurements using U and Th, in addition to other isotopic or magnetic studies would be helpful identifying changes

in dust sources from Sahara Metacraton versus other areas over time. A study of zircons from the entire suite of samples may reveal trends along the west to east transect of their collection points.

The errors of this study highlight paths for improvement. The Munsell system of redness rating is not an ideal method of testing hematite content, though it may be of important field use in an area that is difficult to get data from. Redness ratings using the Munsell system should be paired with visible reflectance spectrometry, and a larger amount of people should be polled for Munsell colors. The particles in this experiment were not as fully disaggregated as intended, thus skewing the results of individual particle chemistry. However, agglomerated particles yielded interesting insights on particles containing both dissolution and precipitation features in a complicated environmental system. Should future studies be performed on more precise chemistry of individual particles, it would be advisable to run the samples through a second disaggregation in the sonicator before mounting them to a stub. The carbon results of EDS were discarded because the stubs were coated with carbon and would mask any carbon content in the grains.

Conclusion

Particles containing magnetic minerals and heavy metals from eight collection sites in Niger and Chad were analyzed for their individual morphology and chemistry. The sites chosen were located along a west-east transect through the Sahel, an area known to be sensitive to changing climate conditions. The purpose of this study was to identify physical and chemical characteristics of magnetic minerals on an individual particle basis and relate them to environmental conditions through Munsell soil color, SEM, and EDS analysis. The particles analyzed were selected based on individual morphological characteristics. Redness ratings, chemistry, and morphology did not exhibit any trends from one collection site to the next along the transect. The results of the natural particles are indicative of weathering conditions that may have been found along the Sahel at the point of collection. The samples are a mixture of red and yellow clays with several particles exhibiting both dissolution and precipitation. Contaminants were found in five of the eight samples. The results of this study, as well as other related studies on these samples, can be used on future collections at the same sites to monitor changes over time. Increases in the redness rating will indicate a more arid environment, while decreases in redness ratings will reflect an environment experiencing an increase in precipitation. Bulk heavy metal analysis on the entire suite of samples may provide details about the fate and transport of TMPs from key sources, such as mining operations and road dust.

Bibliography

Aarons S. M., Aciego S. M. and Gleason J. D. (2013) Variable Hf-Sr-Nd radiogenic isotopic compositions in a Saharan dust storm over the Atlantic: Implications for dust flux to oceans, ice sheets and the terrestrial biosphere. *Chem. Geol.* **349**, 18–26.

Abdelsalam M. G., Liégeois J.-P. and Stern R. J. (2002) The Saharan Metacraton. *J. African Earth Sci.* **34**, 119–136. Available at: www.elsevier.com/locate/jafrearsci.

Akpinar-Elci M., Martin F. E., Behr J. G. and Diaz R. (2015) Saharan dust, climate variability, and asthma in Grenada, the Caribbean. *Int. J. Biometeorol.* **59**, 1667–1671.

Alamirew N. K., Todd M. C., Ryder C. L., Marsham J. H. and Wang Y. (2018) The early summertime Saharan heat low: Sensitivity of the radiation budget and atmospheric heating to water vapour and dust aerosol. *Atmos. Chem. Phys.* **18**, 1241–1262.

Al Jazeera (2010) Nigeria floods displace millions. *Al Jazeera*. Available at: https://www.aljazeera.com/news/africa/2010/09/201092419542142390 1.html.

Amiri-Farahani A., Allen J. R., Neubauer D. and Lohmann U. (2017) Impact of Saharan dust on North Atlantic marine stratocumulus clouds: Importance of the semidirect effect. *Atmos. Chem. Phys.* **17**, 6305–6322.

Arfala Y., Douch J., Assabbane A., Kaaouachi K., Tian H. and Hamdani M. (2018) Assessment of heavy metals released into the air from the cement kilns co-burning waste: Case of Oujda cement manufacturing (Northeast Morocco). *Sustain. Environ. Res.* **28**, 363–373.

Armitage S. J., Bristow C. S. and Drake N. A. (2015) West African monsoon dynamics inferred from abrupt fluctuations of Lake Mega-Chad. *Proc. Natl. Acad. Sci.*, 1–6.

Ayres R. U. (1992) Toxic heavy metals: Materials cycle optimization. *Proc. Natl. Acad. Sci. U. S. A.* **89**, 815–820. Available at: http://www.ncbi.nlm.nih.gov/pubmed/11607259.

Baker A. R. and Jickells T. D. (2006) Mineral particle size as a control on aerosol iron solubility. *Geophys. Res. Lett.* **33**, 1–4.

BBC News (2010) Niger River floods destroying homes and crops. *BBC News*. Available at: https://www.bbc.com/news/world-africa-10929144 [Accessed March 31, 2019].

Beauvais A. and Chardon D. (2013) Modes, tempo, and spatial variability of Cenozoic cratonic denudation: The West African example. *Geochemistry, Geophys. Geosystems* **14**, 1590–1608.

Boose Y., Sierau B., Isabel García M., Rodríguez S., Alastuey A., Linke C., Schnaiter M., Kupiszewski P., Kanji Z. A. and Lohmann U. (2016) Ice nucleating particles in the Saharan Air Layer. *Atmos. Chem. Phys.* **16**, 9067–9087.

Bouchette F., Schuster M., Ghienne J. F., Denamiel C., Roquin C., Moussa A., Marsaleix P. and Duringer P. (2010) Hydrodynamics in Holocene Lake Mega-Chad. *Quat. Res.* **73**, 226–236.

Bouchez C., Goncalves J., Deschamps P., Vallet-Coulomb C., Hamelin B., Doumnang J.-C., Sylvestre F., Bouchez C., Goncalves J., Deschamps P., Vallet-Coulomb C., Hamelin B.,

Doumnang J.-C., Sylvestre F., Bouchez C., Goncalves J., Deschamps P., Vallet-Coulomb C., Hamelin B., Doumnang J.-C. and Sylvestre F. (2016) Hydrological, chemical, and isotopic budgets of Lake Chad: a quantitative assessment of evaporation, transpiration and infiltration fluxes. *Hydrol. Earth Syst. Sci.*

Bourliva A., Papadopoulou L., Aidona E., Giouri K., Simeonidis K. and Vourlias G. (2017) Characterization and geochemistry of technogenic magnetic particles (TMPs) in contaminated industrial soils: Assessing health risk via ingestion. *Geoderma* **295**, 86–97.

Boy J. and Wilcke W. (2008) Tropical Andean forest derives calcium and magnesium from Saharan dust. *Global Biogeochem. Cycles* **22**, 1–11.

Bretl S., Reutter P., Raible C. C., Ferrachat S., Poberaj C. S., Revell L. E. and Lohmann U. (2015) The influence of absorbed solar radiation by Saharan dust on hurricane genesis. *J. Geophys. Res.* **120**, 1902–1917.

Bristow C., Chappell A., Engelstaedter S., Mbainayel S. and Washington R. (2005) *The Bodélé: Dustiest place on Earth*., London.

Bristow C. S. and Armitage S. J. (2016) Dune ages in the sand deserts of the southern Sahara and Sahel. *Quat. Int.* **410**, 46–57.

Bristow C. S., Drake N. and Armitage S. (2009) Deflation in the dustiest place on Earth: The Bodélé Depression, Chad. *Geomorphology* **105**, 50–58.

Brunekreef B. and Forsberg B. (2005) Epidemiological evidence of effects of coarse airborne particles on health. *Eur. Respir. J.* **26**, 309–318.

Bullard J. E., Mctainsh G. H. and Pudmenzky C. (2007) Factors affecting the nature and rate of dust production from natural dune sands. *Sedimentology* **54**, 169–182.

Bullard J. E., McTainsh G. H. and Pudmenzky C. (2004) Aeolian abrasion and modes of fine particle production from natural red dune sands: An experimental study. *Sedimentology* **51**, 1103–1125.

Bullard J. E. and White K. (2005) Dust production and the release of iron oxides resulting from the aeolian abrasion of natural dune sands. *Earth Surf. Process. Landforms* **30**, 95–106.

Bullard J. E. and White K. (2002) Quantifying iron oxide coatings on dune sands using spectrometric measurements: An example from the Simpson-Strzelecki Desert, Australia. *J. Geophys. Res.* **107**, 1–14.

Le Cam M. (2017) Niger floods leave tens of thousands homeless as rebuilding lags. *Reuters*. Available at: https://www.reuters.com/article/us-niger-floods-aid/niger-floods-leave-tens-of-thousands-homeless-as-rebuilding-lags-idUSKCN1BU19Z [Accessed March 31, 2019].

Camêlo D. de L., Ker J. C., Fontes M. P. F., Corrêa M. M., da Costa A. C. S. and Melo V. F. (2017) Pedogenic iron oxides in iron-rich oxisols developed from mafic rocks. *Rev. Bras. Cienc. do Solo* **41**, 1–16.

Chien C. Te, Mackey K. R. M., Dutkiewicz S., Mahowald N. M., Prospero J. M. and Paytan A. (2016) Effects of African dust deposition on phytoplankton in the western tropical Atlantic

Ocean off Barbados. *Global Biogeochem. Cycles* **30**, 716–734.

Chou C., Formenti P., Maille M., Ausset P., Helas G., Harrison M. and Osborne S. (2008) Size distribution, shape, and composition of mineral dust aerosols collected during the African Monsoon Multidisciplinary Analysis Special Observation Period 0: Dust and Biomass-Burning Experiment field campaign in Niger, January 2006. *J. Geophys. Res. Atmos.* **113**, 1–17.

Churchman G. J., Lowe D. J., Huang P. M., Li Y. and Sumner M. E. (2012) Alteration, formation, and occurrence of minerals in soils. In *Handbook of Soil Sciences* CRC Press, Boca Raton. pp. 20–21.

Cockerton H. E., Holmes J. A., Street-Perrott F. A. and Ficken K. J. (2014) Holocene dust records from the West African Sahel and their implications for changes in climate and land surface conditions. *J. Geophys. Res.* **119**, 8684–8694.

Cowie S. M., Knippertz P. and Marsham J. H. (2013) Are vegetation-related roughness changes the cause of the recent decrease in dust emission from the Sahel? *Geophys. Res. Lett.* **40**, 1868–1872.

Coz E., Gómez-Moreno F. J., Pujadas M., Casuccio G. S., Lersch T. L. and Artíñano B. (2009) Individual particle characteristics of North African dust under different long-range transport scenarios. *Atmos. Environ.* **43**, 1850–1863.

Coz E., Moreno T. and Artíñano B. (2011) Variations on the mineralogical particle properties of atmospheric Saharan dust from different source regions. *Rev. la Soc. Española Mineral.* **15**, 69–70.

Crouvi O., Schepanski K., Amit R., Gillespie A. R. and Enzel Y. (2012) Multiple dust sources in the Sahara Desert: The importance of sand dunes. *Geophys. Res. Lett.* **9**, 1–8.

Dearing J. A., Hay K. L., Baban S. M. J., Huddleston A. S., Wellington E. M. H. and Loveland P. J. (1996) Magnetic susceptibility of soil: An evaluation of conflicting theories using a national data set. *Geophys. J. Int.* **127**, 728–734.

Denjean C., Cassola F., Mazzino A., Triquet S., Chevaillier S., Grand N., Bourrianne T., Momboisse G., Sellegri K., Schwarzenbock A., Freney E., Mallet M. and Formenti P. (2016) Size distribution and optical properties of mineral dust aerosols transported in the western Mediterranean. *Atmos. Chem. Phys.* **16**, 1081–1104.

Desboeufs K. V., Losno R., Vimeux F. and Cholbi S. (1999) The pH-dependent dissolution of wind-transported Saharan dust. *J. Geophys. Res. Atmos.* **104**, 21287–21299.

Díaz J., Tobías A. and Linares C. (2012) Saharan dust and association between particulate matter and case-specific mortality: A case-crossover analysis in Madrid (Spain). *Environ. Heal. A Glob. Access Sci. Source* **11**, 1–6.

van der Does M., Knippertz P., Zschenderlein P., Harrison R. G. and Stuut J.-B. W. (2018) The mysterious long-range transport of giant mineral dust particles. *Sci. Adv.* **4**, 1–8.

Dolcater D. L., Syers J. K. and Jackson M. L. (1970) Titanium as free oxide and substituted forms in kaolinites and other soil minerals. *Clays Clay Miner.* **18**, 71–79.

Drake N. and Bristow C. (2006) Shorelines in the Sahara: Geomorphological evidence for an enhanced monsoon from palaeolake Megachad. *The Holocene* **16**, 901–911.

Dunion J. P. and Velden C. S. (2004) The impact of the Saharan air layer on Atlantic tropical cyclone activity. *Bull. Am. Meteorol. Soc.* **85**, 353–366.

Encyclopædia Britannica I. West African Monsoon. Available at: https://www.britannica.com/science/West-African-monsoon [Accessed June 5, 2018].

Engelstaedter S., Tegen I. and Washington R. (2006) North African dust emissions and transport. *Earth-Science Rev.* **79**, 73–100.

Engelstaedter S. and Washington R. (2007) Atmospheric controls on the annual cycle of North African dust. *J. Geophys. Res. Atmos.* **112**, 1–14.

Estokova A., Palascakova L. and Kanuchova M. (2018) Study on Cr(VI) leaching from cement and cement composites. *Int J Env. Res Public Heal.* **15**, 824.

Evan A. T., Fiedler S., Zhao C., Menut L., Schepanski K., Flamant C. and Doherty O. (2015) Derivation of an observation-based map of North African dust emission. *Aeolian Res.* **16**, 153–162.

Evan A. T., Flamant C., Fiedler S. and Doherty O. (2014) An analysis of aeolian dust in climate models. *Geophys. Res. Lett.* **41**, 5996–6001.

Evan T., Flamant C., Gaetani M. and Guichard F. (2016) The past, present and future of African dust. *Nature* **531**, 493–507. Available at: www.nature.com/reprints.

Falkovich A. H. (2004) Adsorption of organic compounds pertinent to urban environments onto mineral dust particles. *J. Geophys. Res.* **109**, 1–19.

Fang H., Cui Z., He G., Huang L. and Chen M. (2017) Phosphorus adsorption onto clay minerals and iron oxide with consideration of heterogeneous particle morphology. *Sci. Total Environ.* **605**–**606**, 357–367.

Farrand M. (1970) Framboidal sulphides precipitated synthetically. *Miner. Depos.* **5**, 237–247.

Fashola M. O., Ngole-Jeme V. M. and Babalola O. O. (2016) Heavy metal pollution from gold mines: Environmental effects and bacterial strategies for resistance. *Int J Env. Res Public Heal.* **13**, 1–20.

Fatoye F. B., Ibitomi M A. and Omada J. I. (2014) Lead-Zinc-Barytes mineralization in the Benue Trough, Nigeria: Their geology, occurrences and economic prospective. *Adv. n Appl. Sci. Res.* **5**, 86–92. Available at: www.pelagiaresearchlibrary.com.

Force E. R., Richards R. P., Scott K. M., Valentine P. C. and Fishman N. S. (1996) Mineral intergrowths replaced by "elbow-twinned" rutile in altered rocks. *Can. Mineral.* **34**, 605–614.

Formenti P., Caquineau S., Desboeufs K., Klaver A., Chevaillier S., Journet E. and Rajot J. L. (2014) Mapping the physico-chemical properties of mineral dust in western Africa: Mineralogical composition. *Atmos. Chem. Phys.* **14**, 10663–10686.

Formenti P., Schütz L., Balkanski Y., Desboeufs K., Ebert M., Kandler K., Petzold A., Scheuvens D., Weinbruch S. and Zhang D. (2011) Recent progress in understanding physical and chemical properties of African and Asian mineral dust. *Atmos. Chem. Phys.* **11**, 8231–8256.

Friese C. A., Van Hateren J. A., Vogt C., Fischer G. and Stuut J. B. W. (2017) Seasonal provenance changes in present-day Saharan dust collected in and off Mauritania. *Atmos. Chem. Phys.* **17**, 10163–10193.

Gao X., Hao Q., Wang L., Oldfield F., Bloemendal J., Deng C., Song Y., Ge J., Wu H., Xu B., Li F., Han L., Fu Y. and Guo Z. (2018) The different climatic response of pedogenic hematite and ferrimagnetic minerals: Evidence from particle-sized modern soils over the Chinese Loess Plateau. *Quat. Sci. Rev.* **179**, 69–86.

García I. M., Van Drooge B. L., Rodríguez S. and Alastuey A. (2017) Speciation of organic aerosols in the Saharan Air Layer and in the free troposphere westerlies. *Atmos. Chem. Phys.* **17**, 8939–8958.

Gherboudj I., Naseema Beegum S. and Ghedira H. (2017) Identifying natural dust source regions over the Middle-East and North-Africa: Estimation of dust emission potential. *Earth-Science Rev.* **165**, 342–355.

Giannadaki D., Pozzer A. and Lelieveld J. (2014) Modeled global effects of airborne desert dust on air quality and premature mortality. *Atmos. Chem. Phys.* **14**, 957–968.

Ginoux P., Prospero J. M., Gill T. E., Hsu N. C. and Zhao M. (2012) Global-scale attribution of anthropogenic and natural dust sources and their emission rates based on MODIS Deep Blue aerosol products. *Rev. Geophys.* **50**, 1–36.

Giorgis I., Bonetto S., Giustetto R., Lawane A., Pantet A., Rossetti P., Thomassin J. H. and Vinai R. (2014) The lateritic profile of Balkouin, Burkina Faso: Geochemistry, mineralogy and genesis. *J. African Earth Sci.* **90**, 31–48.

Google Maps (2019) Nigeria and Chad. Available at: maps.google.com [Accessed April 30, 2018].

Goudie A. S. (2014) Desert dust and human health disorders. *Environ. Int.* **63**, 101–113.

Goudie A. S. (2009) Dust storms: Recent developments. *J. Environ. Manage.* **90**, 89–94.

Goudie A. S. (2008) The history and nature of wind erosion in deserts. *Annu. Rev. Earth Planet. Sci.* **36**, 97–119.

Goudie A. S. and Watson A. (1981) The shape of desert sand dune grains. *J. Arid Environ.* **4**, 185–190.

Griffin D. W. (2007) Atmospheric movement of microorganisms in clouds of desert dust and implications for human health. *Clin. Microbiol. Rev.* **20**, 459–477.

Gross A., Palchan D., Krom M. D. and Angert A. (2016) Elemental and isotopic composition of surface soils from key Saharan dust sources. *Chem. Geol.* **442**, 54–61.

Grousset F. E. and Biscaye P. E. (2005) Tracing dust sources and transport patterns using Sr, Nd

and Pb isotopes. *Chem. Geol.* **222**, 149–167.

Grousset F. E., Parra M., Bory A., Martinez P., Bertrand P., Shimmield-M G. and Ellamn R. M. (1998) Saharan wind regimes traced by the Sr-Nd isotopic composition of subtropical Atlantic sediments: Last Glacial Maximum vs today. *Quat. Sci. Rev.* **17**, 395–409.

Guan H., Zhu C., Zhu T., Wu L. and Li Y. (2016) Grain size, magnetic susceptibility and geochemical characteristics of the loess in the Chaohu lake basin: Implications for the origin, palaeoclimatic change and provenance. *J. Asian Earth Sci.* **117**, 170–183.

Guiraud R., Bosworth W., Thierry J. and Delplanque A. (2005) Phanerozoic geological evolution of Northern and Central Africa: An overview. *J. African Earth Sci.*, 43.

Hereher M. (2011) The Sahara: A desert of change. In *Sand Dunes: Ecology, Geology and Conservation* (ed. C. Galvin). Nova Science, New York. pp. 101–115. Available at: https://www.researchgate.net/publication/266614200.

Hettiarachchi E., Reynolds R. L., Goldstein H. L., Moskowitz B. and Rubasinghege G. (2018) Iron dissolution and speciation in atmospheric mineral dust: Metal-metal synergistic and antagonistic effects. *Atmos. Environ.* **187**, 417–423.

Hunt A., Oldfield F., Bloemendal J., Boyle J. F., Chiverrell R. C., Lyons R., Shen Z., Williams E. R. and Balsam W. (2017) To what extent have laterites contributed to the geochemical, surface reflectance and magnetic properties of adjacent tropical soils? Evidence from Niger and Burkina Faso. *Earth Surf. Process. Landforms* **42**, 2554–2569.

Hurst V. J. (1977) Visual estimation of iron in saprolite. *Bull. Geol. Soc. Am.* **88**, 174–176.

Husar R. B. (2004) *Intercontinental transport of dust: Historical and recent observational evidence*., Springer, Berlin.

Inda A. V., Fink J. R. and Santos T. F. dos (2018) Pedogenic iron oxides in soils of the Acre State, Brazil. *Ciência Rural* **48**, 1–15.

IPCC (2014) *Climate Change 2014: Synthesis Report. Contribution of Working Groups I, II and III to the Fifth Assessment Report of the Intergovernmental Panel on Climate Change*., IPCC, Geneva. Available at: http://www.ipcc.ch.

IRIN (2010) Chad: Flood response challenges in N'Djamena. *Reli. Web*. Available at: https://reliefweb.int/report/chad/chad-flood-response-challenges-ndjamena [Accessed March 15, 2019].

IRIN (2012a) Floods affect tens of thousands. *New Humanit.*

IRIN (2012b) Floods hit hundreds of thousands in Chad after heavy August rains. *Guard.* Available at: https://www.theguardian.com/global-development/2012/sep/11/floods-hit-thousands-chad-rains [Accessed March 15, 2019].

Ito A. and Kok J. F. (2017) Do dust emissions from sparsely vegetated regions dominate atmospheric iron supply to the Southern Ocean? *J. Geophys. Res.* **122**, 3987–4002.

Jiang Z., Liu Q., Dekkers M. J., Barron V., Torrent J. and Roberts A. P. (2016) Control of Earth-like magnetic fields on the transformation of ferrihydrite to hematite and goethite. *Sci. Rep.*

6, 1–11.

Jickells T. D., An Z. S., Andersen K. K., Baker A. R., Bergametti G., Brooks N., Cao J. J., Boyd P. W., Duce R. A., Hunter K. A., Kawahata H., Kubilay N., Laroche J., Liss P. S., Mahowald N., Prospero J. M., Ridgwell A. J., Tegen I. and Torres R. (2005) Global iron connections between desert dust, ocean biogeochemistry, and climate. *Science (80-.).* **308**, 67–71. Available at: http://science.sciencemag.org/.

Jickells T. D., Baker A. R. and Chance R. (2016) Atmospheric transport of trace elements and nutrients to the oceans. *Philos. Trans. R. Soc. A Math. Phys. Eng. Sci.* **374**, 1–19.

Journet E., Desboeufs K. V., Caquineau S. and Colin J. L. (2008) Mineralogy as a critical factor of dust iron solubility. *Geophys. Res. Lett.* **35**, 1–5.

Kaly F., Marticorena B., Chatenet B., Rajot J. L., Janicot S., Niang A., Yahi H., Thiria S., Maman A., Zakou A., Coulibaly B. S., Coulibaly M., Koné I., Traoré S., Diallo A. and Ndiaye T. (2015) Variability of mineral dust concentrations over West Africa monitored by the Sahelian Dust Transect. *Atmos. Res.* **164**, 226–241.

Kandler K., Benker N., Bundke U., Cuevas E., Ebert M., Knippertz P., Rodríguez S., Schütz L. and Weinbruch S. (2007) Chemical composition and complex refractive index of Saharan mineral dust at Izaña, Tenerife (Spain) derived by electron microscopy. *Atmos. Environ.* **41**, 8058–8074.

Kellogg C. A. and Griffin D. W. (2006) Aerobiology and the global transport of desert dust. *Trends Ecol. Evol.* **21**, 638–644.

Kim D., Chin M., Remer L. A., Diehl T., Bian H., Yu H., Brown M. E. and Stockwell W. R. (2017) Role of surface wind and vegetation cover in multi-decadal variations of dust emission in the Sahara and Sahel. *Atmos. Environ.* **148**, 282–296.

Kim D., Chin M., Yu H., Diehl T., Tan Q., Kahn R. A., Tsigaridis K., Bauer S. E., Takemura T., Pozzoli L., Bellouin N., Schulz M., Peyridieu S., Chédin A. and Koffi B. (2014) Sources, sinks, and transatlantic transport of North African dust aerosol: A multimodel analysis and comparison with remote sensing data. *J. Geophys. Res.* **119**, 62599–6277.

Kinne S., Schulz M., Textor C., Guibert S., Balkanski Y., Bauer S. E., Berntsen T., Berglen T. F., Boucher O., Chin M., Collins W., Dentener F., Diehl T., Easter R., Feichter J., Fillmore D., Ghan S., Ginoux P., Gong S., Grini A., Hendricks J., Herzog M., Horowitz L., Isaksen I., Iversen T., Kirkevåg A., Kloster S., Koch D., Kristjansson E., Krol M., Lauer A., Lamarque J. F., Lesins G., Liu X., Lohmann U., Montanaro V., Myhre G., Penner J. E., Pitari G., Reddy S., Seland O., Stier P., Takemura T. and Tie X. (2010) An AeroCom initial assessment – optical properties in aerosol component modules of global models. *Atmos. Chem. Phys. Discuss.* **5**, 1815–1834.

Knippertz P., Ansmann A., Althausen D., Müller D., Tesche M., Bierwirth E., Dinter T., Müller T., Von Hoyningen-huene W., Schepanski K., Wendisch M., Heinold B., Kandler K., Petzold A., Schütz L. and Tegen I. (2009) Dust mobilization and transport in the northern Sahara during SAMUM 2006 - A meteorological overview. *Tellus, Ser. B Chem. Phys. Meteorol.* **61**, 12–31.

Knippertz P., Ansmann A., Althausen D., Müller D., Tesche M., Bierwirth E., Dinter T., Müller T., Von Hoyningen-Huene W., Schepanski K., Wendisch M., Heinold B., Kandler K., Petzold A., Schütz L. and Tegen I. (2007) Dust mobilization due to density currents in the Atlas region: Observations from the Saharan Mineral Dust Experiment 2006 field campaign. *J. Geophys. Res. Atmos.*

Knippertz P. and Todd M. C. (2010) The central west Saharan dust hot spot and its relation to African easterly waves and extratropical disturbances. *J. Geophys. Res. Atmos.* **115**, 1–6.

Kok J. F., Ridley D. A., Zhou Q., Miller R. L., Zhao C., Heald C. L., Ward D. S., Albani S. and Haustein K. (2017) Smaller desert dust cooling effect estimated from analysis of dust size and abundance. *Nat. Geosci.* **10**, 274–278.

Kröner A. and Stern R. J. (2004) Pan-African Orogeny. *Encycl. Geol. vol. 1*, 1–12.

Kuhnert H., Mulitza S., Schulz M., Meyer I., Zabel M., Fischer H. W., Stuut J.-B., Pittauerova D., Mollenhauer G., Heslop D. and Collins J. A. (2010) Increase in African dust flux at the onset of commercial agriculture in the Sahel region. *Nature* **466**, 226–228.

Kumar A., Abouchami W., Galer S. J. G., Singh S. P., Fomba K. W., Prospero J. M. and Andreae M. O. (2018) Seasonal radiogenic isotopic variability of the African dust outflow to the tropical Atlantic Ocean and across to the Caribbean. *Earth Planet. Sci. Lett.* **487**, 94–105.

Lee J. and Lee K. (2013) Effects of Asian dust events on daily asthma patients in Seoul, Korea. *Meteorol. Appl.* **21**, 202–209.

Lenes J. M., Darrow B. A., Walsh J. J., Prospero J. M., He R., Weisberg R. H., Vargo G. A. and Heil C. A. (2008) Saharan dust and phosphatic fidelity: A three-dimensional biogeochemical model of Trichodesmium as a nutrient source for red tides on the West Florida Shelf. *Cont. Shelf Res.* **28**, 1091–1115.

Levin Z., Ganor E. and Gladstein V. (1985) The effects of desert particles coated with sulfate on rain formation. *J. Appl. Meteorol.* **35**, 1511–1523.

Liu Q., Zhang C., Torrent J., Barrón V., Hu P., Jiang Z. and Duan Z. (2016) Factors controlling magnetism of reddish brown soil profiles from calcarenites in Southern Spain: Dust input or in-situ pedogenesis? *Front. Earth Sci. | www.frontiersin.org* **3**, 1–15. Available at: www.frontiersin.org.

Long X., Ji J., Barrón V. and Torrent J. (2016) Climatic thresholds for pedogenic iron oxides under aerobic conditions: Processes and their significance in paleoclimate reconstruction. *Quat. Sci. Rev.* **150**, 264–277.

De Longueville F., Hountondji Y. C., Henry S. and Ozer P. (2010) What do we know about effects of desert dust on air quality and human health in West Africa compared to other regions? *Sci. Total Environ.* **409**, 1–8.

Lopez T., Ramillien G., Antoine R., Darrozes J., Cui Y. J. and Kerr Y. (2018) Investigation of short-term evolution of soil characteristics over the Lake Chad basin using GRACE data. *Remote Sens.* **10**, 1–24.

Luther G. W., Giblin A., Howarth R. W. and Ryans R. A. (1982) Pyrite and oxidized iron mineral phases formed from pyrite oxidation in salt marsh and estuarine sediments. *Geochim. Cosmochim. Acta* **46**, 2665–2669.

Lyons R., Oldfield F. and Williams E. (2010) Mineral magnetic properties of surface soils and sands across four North African transects and links to climatic gradients. *Geochemistry, Geophys. Geosystems* **11**, 1–22.

Lyons R., Oldfield F. and Williams E. (2012) The possible role of magnetic measurements in the discrimination of Sahara/Sahel dust sources. *Earth Surf. Process. Landforms* **37**, 594–606.

Mahecic A. (2010) Flooding in Chad affects 150,000 people including refugees. *UNHCR UN Refug. Agency*. Available at: https://www.unhcr.org/news/briefing/2010/9/4c9359999/chad-torrential-rains-affect-150000-people-including-refugees.html [Accessed March 15, 2019].

Maher B. A., Prospero J. M., Mackie D., Gaiero D., Hesse P. P. and Balkanski Y. (2010) Global connections between aeolian dust, climate and ocean biogeochemistry at the present day and at the last glacial maximum. *Earth-Science Rev.* **99**, 61–97.

Mahowald N. (2011) Aerosol indirect effects on biogeochemistry and climate. *Science (80-.).* **334**, 794–796.

Mahowald N. M., Baker A. R., Bergametti G., Brooks N., Duce R. A., Jickells T. D., Kubilay N., Prospero J. M. and Tegen I. (2005) Atmospheric global dust cycle and iron inputs to the ocean. *Global Biogeochem. Cycles* **19**, 1–15.

Mahowald N. M., Muhs D. R., Levis S., Rasch P. J., Yoshioka M., Zender C. S. and Luo C. (2006) Change in atmospheric mineral aerosols in response to climate: Last glacial period, preindustrial, modern, and doubled carbon dioxide climates. *J. Geophys. Res. Atmos.* **111**, 1–22.

Margolis S. V. and Krinsley D. H. (1971) Submicroscopic frosting on eolian and subaqueous quartz sand grains. *Bull. Geol. Soc. Am.* **82**, 3395–3406.

Marticorena B., Chatenet B., Rajot J. L., Bergametti G., Deroubaix A., Vincent J., Kouoi A., Schmechtig C., Coulibaly M., Diallo A., Koné I., Maman A., Ndiaye T. and Zakou A. (2017) Mineral dust over west and central Sahel: Seasonal patterns of dry and wet deposition fluxes from a pluriannual sampling (2006-2012). *J. Geophys. Res. Atmos.* **122**, 1338–1364.

Masindi V. and Muedi K. L. (2018) Environmental contamination by heavy metals. In *Heavy Metals* InTech. pp. 114–133.

Mather R. L., Reynolds S. E., Wolff G. A., Williams R. G., Torres-Valdes S., Woodward E. M. S., Landolfi A., Pan X., Sanders R. and Achterberg E. P. (2008) Phosphorus cycling in the North and South Atlantic Ocean subtropical gyres. *Nat. Geosci.* **1**, 439–443.

Matin M. M., Hakimi M. and Mazloum-Ardakani M. (2017) The effect of preparation method and presence of impurity on structural properties and morphology of iron oxide. *Islam. Azad Univ. J. Optoelectron. Nanostructures* **2**, 1–8.

McLaughlin R. J. W. (1954) Iron and titanium oxides in soil clays and silts. *Geochim.*

Cosmochim. Acta **5**, 85–96.

Mendez J., Guieu C. and Adkins J. (2010) Atmospheric input of manganese and iron to the ocean: Seawater dissolution experiments with Saharan and North American dusts. *Mar. Chem.* **120**, 34–43.

Menut L., Pérez C., Haustein K., Bessagnet B., Prigent C. and Alfaro S. (2013) Impact of surface roughness and soil texture on mineral dust emission fluxes modeling. *J. Geophys. Res. Atmos.* **118**, 6505–6520.

Merrill R. T. (1975) Magnetic effects associated with chemical changes in igneous rocks. *Geophys. Surv.* **2**, 277–311.

Middleton N. J. (2017) Desert dust hazards: A global review. *Aeolian Res.* **24**, 53–63.

Mileti F. A., Langella G., Prins M. A., Vingiani S. and Terribile F. (2013) The hidden nature of parent material in soils of Italian mountain ecosystems. *Geoderma* **207**, 291–309.

Miller R. L., Cakmur R. V., Perlwitz J., Geogdzhayev I. V., Ginoux P., Koch D., Kohfeld K. E., Prigent C., Ruedy R., Schmidt G. A. and Tegen I. (2006) Mineral dust aerosols in the NASA Goddard Institute for Space Sciences ModelE atmospheric general circulation model. *J. Geophys. Res. Atmos.* **111**, 1–19.

Mills M. M., Ridame C., Davey M., La Roche J. and Geider R. J. (2004) Iron and phosphorus co-limit nitrogen fixation in the eastern tropical North Atlantic. *Nature* **429**, 292–294.

Mindat Mindat.org. Available at: https://www.mindat.org/ [Accessed June 4, 2018].

Moreno T., Querol X., Castillo S., Alastuey A., Cuevas E., Herrmann L., Mounkaila M., Elvira J. and Gibbons W. (2006) Geochemical variations in aeolian mineral particles from the Sahara-Sahel dust corridor. *Chemosphere* **65**, 261–270.

Muhs D. R., Budahn J. R., Prospero J. M. and Carey S. N. (2007) Geochemical evidence for African dust inputs to soils of western Atlantic islands: Barbados, the Bahamas, and Florida. *J. Geophys. Res. Earth Surf.* **112**, 1–26.

Munsell Color (1998) *The Munsell book of color: removable samples in two binders*., Munsell Color, Macbeth Division of Kollmorgen Instruments Corporation, New York.

Ndour M., D'Anna B., George C., Ka O., Balkanski Y., Kleffmann J., Stemmler K. and Ammann M. (2008) Photoenhanced uptake of NO2 on mineral dust: Laboratory experiments and model simulations. *Geophys. Res. Lett.* **35**, 1–5.

OECD (2010) *Sahelian climate: past, current, projections*., Devon.

Okin G. S., Baker A. R., Tegen I., Mahowald N. M., Dentener F. J., Duce R. A., Galloway J. N., Hunter K., Kanakidou M., Kubilay N., Prospero J. M., Sarin M., Surapipith V., Uematsu M. and Zhu T. (2011) Impacts of atmospheric nutrient deposition on marine productivity: Roles of nitrogen, phosphorus, and iron. *Global Biogeochem. Cycles* **25**, 1–10.

Ola-Buraimo A. O. and Abdulganiyu Y. (2017) Palynology and stratigraphy of the Upper Miocene Chad Formation, Bornu Basin, northeastern Nigeria. *J. Palaeogeogr.* **6**, 108–116.

Ortiz-Martínez M. G., Rodríguez-Cotto R. I., Ortiz-Rivera M. A., Pluguez-Turull C. W. and Jiménez-Vélez B. D. (2015) Linking endotoxins, African dust PM10 and asthma in an urban and rural environment of Puerto Rico. *Mediators Inflamm.*, 1–14.

Ozer P., Laghdaf M. B. O. M., Lemine S. O. M. and Gassani J. (2007) Estimation of air quality degradation due to Saharan dust at Nouakchott, Mauritania, from horizontal visibility data. *Water. Air. Soil Pollut.* **178**, 79–87.

Pagotto C., Remy N., Legret M. and LeCloirec P. (2001) *Heavy metal pollution of road dust and roadside soil near a major rural highway*., Selper Ltd.

Pan B., Wang Y., Lin Y., Hsieh J., Logan T., Feng X., Jiang J. H., Yung Y. L. and Zhang R. (2018) Impacts of Saharan dust on Atlantic regional climate and implications for tropical cyclones. *J. Clim.* **31**, 7621–7644. Available at: https://doi.org/10.1175/JCLI-D-16-.

Patey M. D., Achterberg E. P., Rijkenberg M. J. and Pearce R. (2015) Aerosol time-series measurements over the tropical Northeast Atlantic Ocean: Dust sources, elemental composition and mineralogy. *Mar. Chem.* **174**, 103–119.

Pérez N., Pey J., Castillo S., Viana M., Alastuey A. and Querol X. (2008) Interpretation of the variability of levels of regional background aerosols in the Western Mediterranean. *Sci. Total Environ.* **407**, 527–540.

Plumlee G. S. and Ziegler T. L. (2007) Mine Waste. *Sci. Direct*. Available at: https://www.sciencedirect.com/topics/earth-and-planetary-sciences/mine-waste [Accessed April 10, 2019].

Pöhlker M. L., Pöhlker C., Ditas F., Klimach T., Hrabe de Angelis I., Araújo A., Brito J., Carbone S., Cheng Y., Chi X., Ditz R., Gunthe S. S., Kesselmeier Jürgen, Könemann T., Lavrič J. V., Martin S. T., Mikhailov E., Moran-Zuloaga D., Rose D., Saturno J., Su H., Thalman R., Walter D., Wang J., Wolff S., Barbosa H. M. J., Artaxo P., Andreae M. O. and Pösch U. (2016) Long-term observations of cloud condensation nuclei in the Amazon rain forest – Part 1: Aerosol size distribution, hygroscopicity, and new model parametrizations for CCN prediction. *Atmos. Chem. Phys.* **16**, 15709–15740.

Powell C. F., Baker A. R., Jickells T. D., Bange H. W., Chance R. J. and Yodle C. (2015) Estimation of the atmospheric flux of nutrients and trace metals to the eastern tropical North Atlantic Ocean. *J. Atmos. Sci.* **72**, 4029–4045.

Preetz H., Igel J., Hannam J. A. and Stadler S. (2017) Relationship between magnetic properties and reddening of tropical soils as indicators of weathering. *Geoderma* **303**, 143–149.

Prospero J. M., Blades E., Naidu R., Mathison G., Thani H. and Lavoie M. C. (2008) Relationship between African dust carried in the Atlantic trade winds and surges in pediatric asthma attendances in the Caribbean. *Int. J. Biometeorol.* **52**, 823–832.

Prospero J. M., Collard F. X., Molinié J. and Jeannot A. Characterizing the annual cycle of African dust transport to the Caribbean Basin and South America and its impact on the environment and air quality. *Global Biogeochem. Cycles* **28**, 757–773.

Prospero J. M., Glaccum R. A. and Nees R. T. (1981) Atmospheric transport of soil dust from Africa to South America. *Nature* **289**, 570–572.

Pulido-Villena E., Wagener T. and Guieu C. (2008) Bacterial response to dust pulses in the western Mediterranean: Implications for carbon cycling in the oligotropic ocean. *Global Biogeochem. Cycles* **22**, 1–12.

Querol X., Pey J., Pandolfi M., Alastuey A., Cusack M., Pérez N., Moreno T., Viana M., Mihalopoulos N., Kallos G. and Kleanthous S. (2009) African dust contributions to mean ambient PM10 mass-levels across the Mediterranean Basin. *Atmos. Environ.* **43**, 4266–4277.

Quist-Arcton O. (2010) In grip of drought, floods, Niger faces hunger crisis. *Natl. Public Radio Morning Ed.* Available at: https://www.npr.org/templates/story/story.php?storyId=129316900 [Accessed April 3, 2019].

Ravelo-Pérez L. M., Rodríguez S., Galindo L., García M. I., Alastuey A. and López-Solano J. (2016) Soluble iron dust export in the high altitude Saharan Air Layer. *Atmos. Environ.* **133**, 49–59.

Ridley D. A., Heald C. L. and Prospero J. M. (2014) What controls the recent changes in African mineral dust aerosol across the Atlantic? *Atmos. Chem. Phys.* **14**, 5735–5747.

Rizzo L. V., Artaxo P., Müller T., Wiedensohler A., Paixão M., Cirino G. G., Arana A., Swietlicki E., Roldin P., Fors E. O., Wiedemann K. T., Leal L. S. M. and Kulmala M. (2013) Long term measurements of aerosol optical properties at a primary forest site in Amazonia. *Atmos. Chem. Phys.* **13**, 2391–2413.

Rizzolo J. A., Barbosa C. G. G., Borillo G. C., Godoi A. F. L., Souza R. A. F., Andreoli R. V., Manzi A. O., Sá M. O., Alves E. G., Pöhlker C., Angelis I. H., Ditas F., Saturno J., Moran-Zuloaga D., Rizzo L. V., Rosário N. E., Pauliquevis T., Santos R. M. N., Yamamoto C. I., Andreae M. O., Artaxo P., Taylor P. E. and Godoi R. H. M. (2017) Soluble iron nutrients in Saharan dust over the central Amazon rainforest. *Atmos. Chem. Phys.* **17**, 2673–2687.

Roberts A. P. and Turner G. M. (1993) Diagenetic formation of ferrimagnetic iron sulphide minerals in rapidly deposited marine sediments, South Island, New Zealand. *Earth Planet. Sci. Lett.* **115**, 257–273.

Rocha-Lima A., Vanderlei Martins J., Remer L. A., Todd M., Marsham J. H., Engelstaedter S., Ryder C. L., Cavazos-Guerra C., Artaxo P., Colarco P. and Washington R. (2018) A detailed characterization of the Saharan dust collected during the Fennec campaign in 2011: In situ ground-based and laboratory measurements. *Atmos. Chem. Phys.* **18**, 1023–1043.

Rodríguez-Cotto R. I., Ortiz-Martínez M. G. and Jiménez-Vélez B. D. (2015) Organic extracts from African dust storms stimulate oxidative stress and induce inflammatory responses in human lung cells through Nrf2 but not NF-κB. *Environ. Toxicol. Pharmacol.* **39**, 845–856.

Ryan P. (2014) *Environmental and low temperature geochemistry*. 1st ed., Wiley, West Sussex.

Schepanski K., Merkel U. and Tegen I. (2014) Mineral dust: Meteorological controls and climate impacts. *Pages Mag.* **22**, 62–63.

Schepanski K., Tegen I., Todd M. C., Heinold B., Bönisch G., Laurent B. and Macke A. (2009) Meteorological processes forcing Saharan dust emission inferred from MSG-SEVIRI

observations of subdaily dust source activation and numerical models. *J. Geophys. Res. Atmos.* **114**, 1–18.

Scheuvens D., Schütz L., Kandler K., Ebert M. and Weinbruch S. (2013) Bulk composition of northern African dust and its source sediments - A compilation. *Earth-Science Rev.* **116**, 170–194.

Schewe J. and Levermann A. (2017) Non-linear intensification of Sahel rainfall as a possible dynamic response to future warming. *Earth Syst. Dyn.* **8**, 495–505.

Schuster M., Duringer P., Ghienne J.-F., Roquin C., Sepulchre P., Moussa A., Lebatard A.-E., Mackaye H. T., Likius A., Vignaud P. and Brunet M. (2009) Chad Basin: Paleoenvironments of the Sahara since the Late Miocene. *Comptes Rendus Geosci.* **341**, 603–611.

Schwarz T. and Germann K. (1999) Weathering surfaces, laterite-derived sediments and associated mineral deposits in north-east Africa. *Palaeoweathering, Palaeosurfaces Relat. Cont. Depos.* **27**, 367–390.

Schwertman U. (1988) Occurrence and formation of iron oxides in various pedoenvironments. In *Iron in soils and clay minerals* Springer Netherlands, Dordrecht. pp. 267–308.

Schwertmann U. (1988) Occurrence and formation of iron oxides in various pedoenvironments. In *Iron in soils and clay minerals* (eds. J. W. Stucki, B. A. Goodman, and U. Schwertmann). D. Reidel Publishing Company, Dordrecht. pp. 267–308.

Schwertmann U. (1985) The effect of pedogenic environments on iron oxide minerals. In *Advances in Soil Science, vol. 1* (ed. B. A. Stewart). Springer-Verlag, New York. pp. 171–200.

Semeniuk T. A., Wise M. E., Martin S. T., Russell L. M. and Buseck P. R. (2007) Water uptake characteristics of individual atmospheric particles having coatings. *Atmos. Environ.* **41**, 6225–6235.

Shao Y., Wyrwoll K. H., Chappell A., Huang J., Lin Z., McTainsh G. H., Mikami M., Tanaka T. Y., Wang X. and Yoon S. (2011) Dust cycle: An emerging core theme in Earth system science. *Aeolian Res.* **2**, 181–204.

Al Shehhi M. R., Gherboudj I. and Ghedira H. (2014) An overview of historical harmful algae blooms outbreaks in the Arabian Seas. *Mar. Pollut. Bull.* **86**, 314–324.

Shellnutt J. G., Pham N. H. T., Denyszyn S. W., Yeh M. W. and Lee T. Y. (2017) Timing of collisional and post-collisional Pan-African Orogeny silicic magmatism in south-central Chad. *Precambrian Res.* **301**, 113–123.

Shinn E. A., Smith G. W., Prospero J. M., Betzer P., Hayes M. L., Garrison V. and Barber R. T. (2000) African dust and the demise of Caribbean coral reefs. *Geophys. Res. Lett.* **27**, 3029–3032.

Smith D. J., Jaffe D. A., Birmele M. N., Griffin D. W., Schuerger A. C., Hee J. and Roberts M. S. (2012) Free tropospheric transport of microorganisms from Asia to North America. *Microb. Ecol.* **64**, 973–985.

Sokolik I. N. and Toon O. B. (1999) Incorporation of mineralogical composition into models of the radiative properties of mineral aerosol from UV to IR wavelengths. *J. Geophys. Res. Atmos.* **104**, 9423–9444.

Strong J. D. O., Vecchi G. A. and Ginoux P. (2018) The climatological effect of Saharan dust on global tropical cyclones in a fully coupled GCM. *J. Geophys. Res. Atmos.* **123**, 5538–5559.

Stuut J. W. and Prins M. A. (2014) The significance of particle size of long-range transported mineral dust. *Pages Mag.* **22**, 70–71.

Su N., Yang S. Y., Wang X. D., Bi L. and Yang C. F. (2015) Magnetic parameters indicate the intensity of chemical weathering developed on igneous rocks in China. *Catena* **133**, 328–341.

Tegen I., Werner M., Harrison S. P. and Kohfeld K. (2004) Relative importance of climate and land use in determining present and future global soil dust emission. *Geophys. Res. Lett.* **31**, 1–4.

Thomas N. and Nigam S. (2018) Twentieth-century climate change over Africa: Seasonal hydroclimate trends and sahara desert expansion. *J. Clim.* **31**, 3349–3370.

Todd M. C., Washington R., Martins J. V., Dubovik O., Lizcano G., M'Bainayel S. and Engelstaedter S. (2007) Mineral dust emission from the Bodélé Depression Nothern Chad, during BoDEx 2005. *J. Geophys. Res. Atmos.* **112**, 1–12.

Torrent J., Schwertmann U. and Schulze D. . G. (1980) Iron oxide mineralogy of some soils of two river terrace sequences in Spain. *Geoderma* **23**, 191–208.

Trezza M. A. and Scian A. N. (2007) Waste with chrome in the Portland cement clinker production. *J Hazard Mater* **147**, 188–196.

U.S. Geological Survey West Africa: Land use and land cover dynamics. Available at: https://eros.usgs.gov/westafrica/node/147 [Accessed February 14, 2019].

United Nations Environment Programme (2018) The tale of a disappearing lake. Available at: https://www.unenvironment.org/news-and-stories/story/tale-disappearing-lake [Accessed February 24, 2019].

Waeles M., Baker A. R., Jickells T. and Hoogewerff J. (2007) Global dust teleconnections: Aerosol iron solubility and stable isotope composition. *Environ. Chem.* **4**, 233–237.

Walsh J. J., Jolliff J. K., Darrow B. P., Lenes J. M., Milroy S. P., Remsen A. D. D. A., Carder K. L., Chen F. R., Vargo G. A., Weisberg R. H., Fanning K. A., Muller-Karger F. E., Shinn E., Steidinger K. A., Heil C. A., Tomas C. R., Prospero J. S., Lee T. N., Kirkpatrick G. J., Whitledge T. E., Stockwell D. A., Villareal T. A., Jochens A. E. and Bontempi P. S. (2006) Red tides in the Gulf of Mexico; where, when, and why? *J. Geophys. Res. Ocean.* **111**, 1–46.

Warren A., Chappell A., Todd M. C., Bristow C., Drake N., Engelstaedter S., Martins V., M'bainayel S. and Washington R. (2007) Dust-raising in the dustiest place on earth. *Geomorphology* **92**, 35–37.

Washington R. (2006) Dust Storms, The Cold War and the Battle of Chicha. Available at: https://www.geog.ox.ac.uk/research/climate/projects/bodex/wardust.html.

Washington R., Bouet C., Cautenet G., Mackenzie E., Ashpole I., Engelstaedter S., Lizcano G., Henderson G. M., Schepanski K. and Tegen I. (2009) Dust as a tipping element: The Bodélé Depression, Chad. *Proc. Natl. Acad. Sci.* **106**, 1–8.

Washington R. and Todd M. C. (2005) Atmospheric controls on mineral dust emission from the Bodélé Depression, Chad: The role of the low level jet. *Geophys. Res. Lett.* **32**, 1–5.

Washington R., Todd M. C., Engelstaedter S., Mbainayel S. and Mitchell F. (2006a) Dust and the low-level circulation over the Bodélé Depression, Chad: Observations from BoDEx 2005. *J. Geophys. Res. Atmos.* **111**, 1–15.

Washington R., Todd M. C., Lizcano G., Tegen I., Flamant C., Koren I., Ginoux P., Engelstaedter S., Bristow C. S., Zender C. S., Goudie A. S., Warren A. and Prospero J. M. (2006b) Links between topography, wind, deflation, lakes and dust: The case of the Bodélé Depression, Chad. *Geophys. Res. Lett.* **33**, 1–4.

Westrich J. R., Ebling A. M., Landing W. M., Joyner J. L., Kemp K. M., Griffin D. W. and Lipp E. K. (2016) Saharan dust nutrients promote Vibrio bloom formation in marine surface waters. *Natl. Acad. Sci.* **113**, 5964–5969.

Williams R. H., McGee D., Kinsley C. W., Ridley D. A., Hu S., Fedorov A., Tal I., Murray R. W. and Demenocal P. B. (2016) Glacial to Holocene changes in trans-Atlantic Saharan dust transport and dust-climate feedbacks. *Sci. Adv.* **2**, 1–11.

Winckler G. and Mahowald N. (2014) DICE: Dust impact on climate and environment. *Pages Mag.* **22**, 61.

Wu L. (2007) Impact of Saharan air layer on hurricane peak intensity. *Geophys. Res. Lett.* **34**, 1–5.

Yang W., Marshak A., Kostinski A. B. and Várnai T. (2013) Shape-induced gravitational sorting of Saharan dust during transatlantic voyage: Evidence from CALIOP lidar depolarization measurements. *Geophys. Res. Lett.* **40**, 3281–3286.

Yu H., Chin M., Bian H., Yuan T., Prospero J. M., Omar A. H., Remer L. A., Winker D. M., Yang Y., Zhang Y. and Zhang Z. (2015a) Quantification of trans-Atlantic dust transport from seven-year (2007-2013) record of CALIPSO lidar measurements. *Remote Sens. Environ.* **159**, 232–249.

Yu H., Chin M., Yuan T., Bian H., Remer L. A., Prospero J. M., Omar A., Winker D., Yang Y., Zhang Y., Zhang Z. and Zhao C. (2015b) The fertilizing role of African dust in the Amazon rainforest: A first multiyear assessment based on data from Cloud-Aerosol Lidar and Infrared Pathfinder Satellite Observations. *Geophys. Res. Lett.* **42**, 1984–1991.

Zhao C., Liu X., Leung L. R. and Hagos S. (2011) Radiative impact of mineral dust on monsoon precipitation variability over West Africa. *Atmos. Chem. Phys.* **11**, 1879–1893.

Zhao W., Balsam W., Williams E., Long X. and Ji J. (2018) Sr–Nd–Hf isotopic fingerprinting of transatlantic dust derived from North Africa. *Earth Planet. Sci. Lett.* **486**, 23–31.